

Correction of dysregulated lipid metabolism normalizes gene expression in oligodendrocytes and prolongs lifespan in female poly-GA C9orf72 mice

Received: 13 March 2024

Accepted: 27 March 2025

Published online: 11 April 2025

 Check for updates

A list of authors and their affiliations appears at the end of the paper

Clinical and genetic research links altered cholesterol metabolism with ALS development and progression, yet pinpointing specific pathomechanisms remain challenging. We investigated how cholesterol dysmetabolism interacts with protein aggregation, demyelination, and neuronal loss in ALS. Bulk RNAseq transcriptomics showed decreased cholesterol biosynthesis and increased cholesterol export in ALS mouse models (GA-Nes, GA-Camk2a GA-CFP, rNLS8) and patient samples (spinal cord), suggesting an adaptive response to cholesterol overload. Consequently, we assessed the efficacy of the cholesterol-binding drug 2-hydroxypropyl- β -cyclodextrin (CD) in a fast-progressing C9orf72 ALS mouse model with extensive poly-GA expression and myelination deficits. CD treatment normalized cholesteryl ester levels, lowered neurofilament light chain levels, and prolonged lifespan in female but not male GA-Nes mice, without impacting poly-GA aggregates. Single nucleus transcriptomics indicated that CD primarily affected oligodendrocytes, significantly restored myelin gene expression, increased density of myelinated axons, inhibited the disease-associated oligodendrocyte response, and downregulated the lipid-associated genes *Plin4* and *ApoD*. These results suggest that reducing excess free cholesterol in the CNS could be a viable ALS treatment strategy.

In amyotrophic lateral sclerosis (ALS), the degeneration of both cortical and spinal motor neurons leads to progressive paralysis and eventually respiratory failure^{1,2}. All sporadic and most genetic cases show cytoplasmic aggregates of the nuclear RNA-binding protein TDP-43, found predominantly in neurons and less frequently in oligodendrocytes playing a key role in neurodegeneration and neuroinflammation^{3–5}. About 5–10% of ALS cases are caused by an (G₄C₂)_n repeat expansion in the first intron of *C9orf72*, which is translated by a non-canonical mechanism in all reading frames into five dipeptide repeat (DPR) proteins co-aggregating in neurons^{6–10}. The most abundant form is poly-GA, which was shown to contribute to TDP-43 aggregation¹¹.

Secondary to neuron loss, ALS patients show demyelination in the motor cortex, corticospinal tract, and the ventral horn of the spinal cord^{12,13}, suggesting that oligodendrocyte dysfunction may affect disease progression. Recently, oligodendrocytes have been linked to a number of neurodegenerative diseases, including Alzheimer's disease^{14–16} and ALS¹⁷. This is further supported by the recent identification of a shared gene expression signature in myelinating oligodendrocytes, termed disease-associated oligodendrocytes (DOLs), in mouse models of Alzheimer's disease and multiple sclerosis^{14,18–21}.

The myelin sheath is a lipid-rich multilayered plasma membrane extension of oligodendrocytes with a particularly high content of

✉ e-mail: dieter.edbauer@dzne.de

cholesterol²². Myelin debris is cleared by microglia, but cholesterol cannot be fully degraded and may accumulate in cholesterol crystals or lipid droplets, leading to “foam cell” formation in primary demyelinating diseases. Effective remyelination requires cholesterol clearance and efflux by microglia²³, which uses ApoE lipoproteins as the major lipid carrier. The common ApoE4 allele is a major risk factor for Alzheimer’s disease. Interestingly, ApoE4 promotes cholesterol deposition in oligodendrocytes, which can also be reversed by 2-hydroxypropyl- β -cyclodextrin (hereafter referred to as CD) treatment in cells and animals¹⁵. Cyclodextrins are cyclic oligosaccharides that increase the cholesterol solubility and excretion. CD is beneficial in experimental models of atherosclerosis²⁴ and was clinically tested in Niemann Pick disease Type C1, but side effects of intrathecal injection were not tolerated²⁵. Currently, a new formulation of CD is tested clinically in Niemann Pick disease and Alzheimer’s disease. Presumably through improved cholesterol clearance, cyclodextrins can also have anti-inflammatory effects²⁴.

Epidemiological studies reveal the complexity of cholesterol metabolism in ALS²⁶. Large longitudinal studies show that ALS patients typically exhibit higher LDL cholesterol levels before onset²⁷ and that increased HDL cholesterol levels are associated with a reduced ALS risk²⁸. Interestingly, at diagnosis, higher LDL levels are associated with slower disease progression and improved survival²⁹. However, these findings could be influenced by factors like ALS-associated weight loss, hypermetabolism, and the survival benefits of a high-calorie diet^{30,31}. Additionally, the cholesterol hydroxylase gene CYP27A1 has been genetically linked to ALS^{32,33}.

Motivated by a transcriptional signature of cholesterol overload in several ALS mouse models and ALS patient spinal cord, we tested the therapeutic potential of CD in our fast-progressing model for C9orf72 ALS, expressing GFP-(GA)₁₇₅ using Nestin-Cre (“GA-Nes”) ³⁴. This mouse line shows widespread poly-GA aggregates throughout the CNS, regional neuron loss, and microglia infiltration, leading to progressive weakness and weight loss. While poly-GA is expressed throughout the CNS, neurodegeneration starts in the hippocampal CA2 region and reaches spinal cord motor neurons at the endstage³⁴. GA-Nes mice reach the humane endpoint at 6–7 weeks of age under national animal welfare laws³⁴. Importantly, CD treatment extends the lifespan in female but not male mice. Single-cell transcriptomics of female mice suggests that poly-GA expression using the Nestin-Cre driver affects almost all cell types in the brain. Interestingly, the oligodendrocytes express several marker genes identified in DOLs in Alzheimer models¹⁴, as well as ApoD and Plin4, which are tightly linked to lipid and cholesterol biology. CD treatment partially reverts the DOL signature and reduces Plin4 expression at the mRNA and protein level arguing for a beneficial effect of targeting altered lipid metabolism in the most common form of familial ALS.

Results

CD extends lifespan and reduces Neurofilament levels in female GA-Nes mice

Comparing our published gene expression datasets from two poly-GA mouse models (GA-Nes with widespread expression throughout the CNS and GA-CFP with expression mostly restricted to spinal neurons), the rNLS8 mouse line expressing TDP-43 Δ NLS, and an updated large dataset of human ALS tissue^{34–37} revealed a common signature of cholesterol dysmetabolism. Bulk RNAseq data (Fig. 1a) showed a reduction of key enzymes in the cholesterol biosynthesis pathway (e.g., Hmgcs1, Hmgcr), accompanied by an induction of the reverse cholesterol export pathway (Abca1, Abcg1). In addition, enzymes for cholesterol esterification (Soat1) and factors critical for lipid droplet formation (Plin2, Plin4) were upregulated, alongside several lipoproteins (ApoE, ApoD, ApoC1). We confirmed our findings in unpublished dataset from independent cohorts of GA-CFP mice and rNLS8 mice (Fig. 1a). While we found no C9orf72-specific changes comparing

C9orf72 ALS and sporadic ALS cases, the cholesterol dysregulation signature was significantly more pronounced in male ALS patients. These changes suggest that overexpression of aggregating poly-GA and TDP-43 in mice leads to cholesterol overload, mirroring findings in the ALS spinal cord.

To test whether cholesterol overload contributes to ALS pathogenesis, we treated our rapidly progressive GA-Nes mouse model with 2-hydroxypropyl- β -cyclodextrin (hereafter referred to as CD). We administered CD (s.c. 2 g/kg) from weaning on postnatal day 21 daily until the humane endpoint was reached by weight loss or muscle weakness according to our standardized scoring system. The dose is in line with previous studies, but we administered CD daily rather than once or twice a week due to the fast progression in this mouse model^{24,25}. Vehicle-treated male and female mice reached the endpoint at a median age of 41 and 43 days, respectively, in line with our initial characterization of this line (Fig. 1b, c)³⁴. In contrast, half of the female GA-Nes mice receiving CD survived beyond 52 days (Fig. 1c). Possibly due to faster progression or due to pro-myelinating effects of testosterone³⁸ or due to differential lipid metabolism between genders, CD was much less beneficial in males, aligning with prior findings in female NPC mice³⁹. These beneficial effects in female GA-Nes mice are reflected in a slower decline of body weight (Fig. S1).

To investigate the mechanism of CD-mediated lifespan extension, we used a second cohort of female GA-Nes treated from day 21 onwards and selected a fixed time point (postnatal day 40) for all further experiments to allow direct comparison in this rapidly progressing mouse model. Male and female transgenic mice showed strong upregulation of serum neurofilament light chain levels (Fig. 1d, e). This phenotype was significantly reduced by approximately 50% upon CD treatment in female GA-Nes mice (Fig. 1e), suggesting that CD attenuates neurodegeneration. In contrast, no such reduction was observed in CD-treated male mice (Fig. 1d), which aligns with the lack of survival benefits. Thus, we conducted all further experiments performed on GA-Nes mice solely on females.

CD treatment had no significant effect on the widespread poly-GA expression in GA-Nes mice (Fig. 1f, g). In contrast to previous immunohistochemistry characterization of poly-GA aggregates in paraffinized tissue, which was predominantly neuronal³⁴, GFP-(GA)₁₇₅ expression was detected in most oligodendrocytes and astrocytes, but only a small subset of microglia in the cryosections imaged using native GFP fluorescence (Figs. 1f and S2), which is consistent with broad excision of the floxed stop cassette in the transgene due to widespread Nestin-Cre expression.

Taken together, GA-Nes mice show signs of cholesterol overload, and in female mice, life span is extended by daily treatment with the cholesterol-sequestering drug CD.

CD mitigates poly-GA induced expression changes in oligodendrocytes

Since CD is known to have pleiotropic effects not only on cholesterol but also on inflammation, we conducted single-cell transcriptomics in the hippocampus of female mice at postnatal day 40 to investigate the mode of action. To facilitate comparison with emerging datasets from human ALS and FTD tissues, we chose to analyze single nuclei from frozen tissue. We prioritized the hippocampus for snRNA-seq, because neurodegeneration occurs first in the CA2 region and remains most pronounced there at the government-mandated humane endpoint³⁴. Using flow cytometry, we isolated 10,000 DAPI-labeled nuclei per animal, 50% of which were NeuN-positive neurons and 50% were NeuN-negative glia (Fig. S3). The nuclei were processed on the 10X platform (Chromium Single Cell 3’ Chip G v3.1). Metrics such as nuclei per sample, reads per nucleus, and reads per gene were consistent across all animals (Fig. S3a). After quality control, our dataset includes 90,772 nuclei from 8 animals in the wildtype condition and 66,263 nuclei from 7 animals in the transgenic condition (Supplementary Data 1).

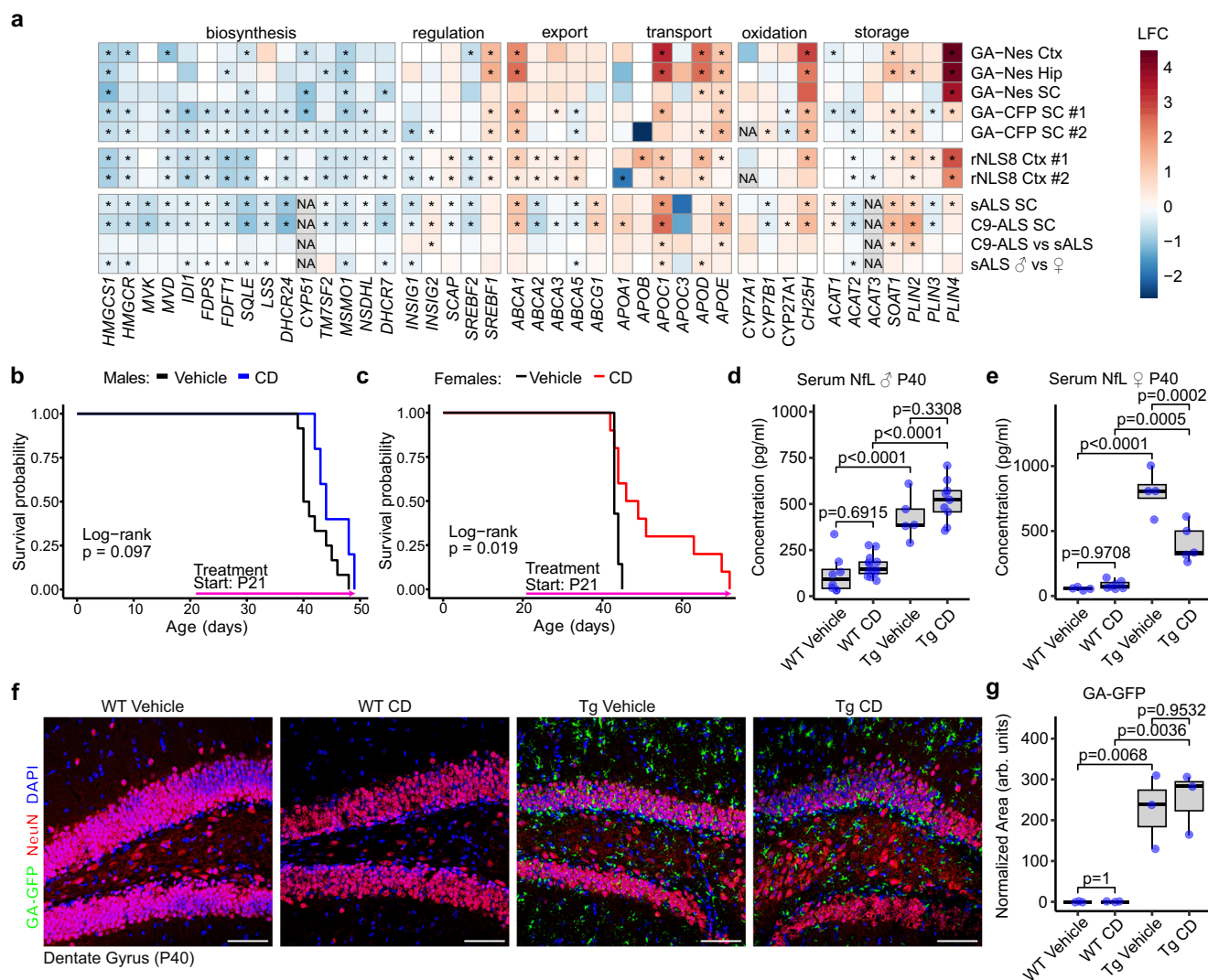


Fig. 1 | Cyclodextrin extends lifespan and reduces Neurofilament levels in female GA-Nes mice. a Gene expression changes in the cholesterol pathway from historical bulk RNAseq dataset in GA-Nes (endstage hippocampus, cortex and spinal cord, 5 control vs 5 GA-Nes mice), GA-CFP (thoracic spinal cord, cohort #1 with 4 wildtype vs. 3 GA-CFP mice 32 weeks of age, cohort #2 with 7 wildtype vs. 6 GA-CFP mice 42 weeks of age) and rNLS8 (hippocampus, after 3 weeks of transgene induction, cohort #1 with 17 wildtype vs. 10 rNLS8 mice, cohort #2 with 11 wildtype and 10 rNLS8 mice) ALS mouse models and patient spinal cord^{34,37,51}. Log₂ fold changes compared to controls are shown in the heat map. Adjusted *p* values from the original analysis are shown because different genotype and species prevent a combined re-analysis with common RNAseq pipelines. Asterisks indicate significant changes. Upregulation of export pathway genes and down-regulation of synthesis genes suggest cholesterol overload. **b** Survival analysis by Kaplan-Meier curve shows that CD administered at 2 g/kg q.d. does not affect the survival of transgenic male mice significantly (*p* = 0.097 from log-rank test for

survival, *n* = 12 vehicle vs 5 CD). **c** Survival analysis by Kaplan-Meier curve shows that CD administered at 2 g/kg q.d. significantly improves the survival of transgenic female mice (*p* = 0.019 from log-rank test for survival, *n* = 7 vehicle vs 10 CD). **d, e** Serum NFL from independent cohorts of mice sacrificed at postnatal day 40 (P40) shows significant modulations (female *n* from independent biological replicates: WT Vehicle = 4, WT CD = 7, Tg Vehicle = 4, Tg CD = 5; male *n* of independent biological replicates: WT Vehicle = 8, WT CD = 15, Tg Vehicle = 5, Tg CD = 9). Post-hoc analysis by Tukey's HSD shows a dramatic increase in transgenic mice, which is partially rescued by CD treatment in female but not male mice. CD administration does not modulate wild-type NFL levels. **f, g** Fluorescence microscopy of endogenous GA-GFP in frozen tissue confirms its neuronal and glial expression in transgenic mice and the lack of expression in wild-type mice, while also highlighting no significant reduction upon CD treatment (ANOVA, post hoc by Tukey's HSD from three independent biological replicates in each group). All scale bars = 75 μm.

Clustering of all cells revealed two states of microglia (proliferating vs. non-dividing), four states of oligodendrocytes (OPC, newly formed oligodendrocytes and myelinating Oligo_mat1 and Oligo_mat2) and 18 subtypes of neurons (Fig. 2a). The expression of the five best marker genes per cluster is shown in Fig. S4, with the absolute number of cells per cluster detailed in Supplementary Data 1.

Although the comparison of cell numbers is limited by the NeuN-based enrichment strategy, it is clear that poly-GA expression strongly increased the number of microglia, including a proliferating subcluster (Figs. 2a and S4, S5, Microglia_div, top markers: Rad51b, Ly86, Atad2, Diaph3, Lrmda). This resulted in an undersampling of other glia, with

an apparent lower abundance of astrocytes and oligodendrocytes. Importantly, our histological quantification of cell density in Fig. S6 shows a ~5-fold increase in Iba1⁺ microglia, which was not significantly affected by CD treatment. While oligodendrocyte numbers were not unaffected by poly-GA expression or CD treatment, the number of S100β-positive astrocytes was even slightly increased in GA-Nes mice, with a trend towards reduction upon CD treatment. Rare clusters of macrophages and other immune cells (B cells, T cells, and a few NK cells) also appeared highly enriched in poly-GA expressing mice in our snRNAseq analysis (Fig. S6). In addition, the relative number of nuclei in the prominent neuroblast population at postnatal day 40 was

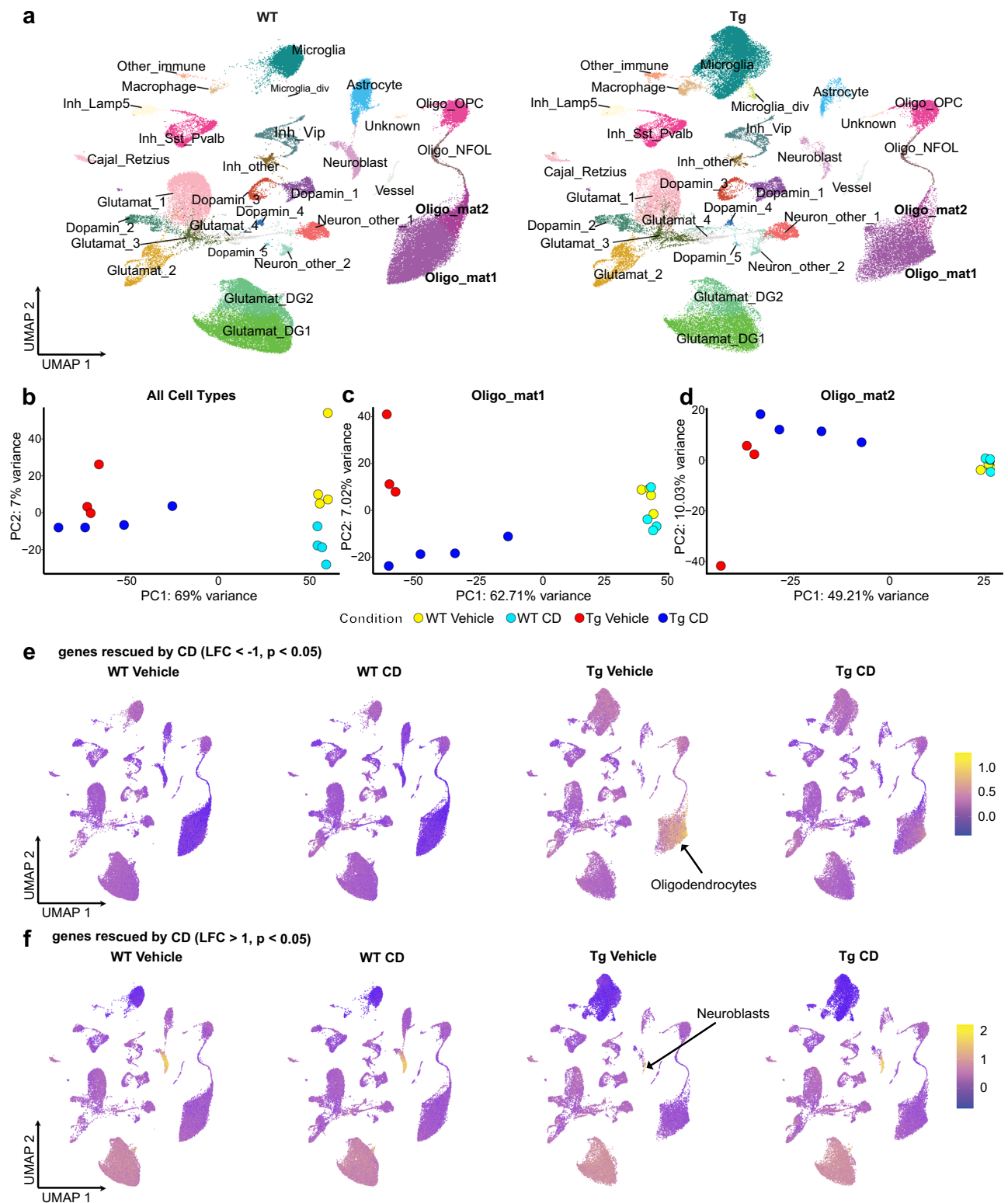


Fig. 2 | snRNAseq highlights oligodendrocytes as target of CD therapy by downregulation of genes. a snRNAseq dimensional reduction plot (UMAP) of WT (90,772 cells from 8 animals) and Tg (66,263 cells from 7 animals) highlights dramatic changes in glial cells. **b** PCA of all expressed genes by combining all clusters clearly separates the genotypes and partially resolves effects by CD treatment. **c, d** PCA of all expressed genes in Oligo_mat1 and Oligo_mat2 clusters, respectively,

highlights the rescue effect of CD treatment in the clusters of mature oligodendrocytes. **e** FeaturePlot of genes combined with AddModuleScore that are downregulated (LFC < -1, adjusted $p < 0.05$) by CD treatment shows that the target of such therapy is primarily oligodendrocytes. **f** FeaturePlot of genes with color-coded AddModuleScore that are upregulated (LFC > 1, adjusted $p < 0.05$) by CD treatment shows that the target of such therapy is primarily neuroblasts.

reduced in GA-Nes mice (Fig. S5). Quantification of neuroblasts with DCX immunofluorescence confirmed a ~80% loss of neuroblasts in GA-Nes mice, which was not rescued by CD treatment (Fig. S6). In line with previous findings, we also detected pronounced neuron loss in the hippocampal CA2 region, which was, however, not significantly rescued by CD treatment (Fig. S6).

Principal component analysis (PCA) analysis of all cell types distinctly separated wild-type and transgenic mice (Fig. 2b and Supplementary Data 2) in the first component, as well as treated and untreated mice in the first and second components. The clustering of CD and vehicle-treated GA-Nes mice was most evident for the mature oligodendrocyte clusters (Fig. 2c, d) and less prominent for other cell types (Fig. S7). Interestingly, transgenic and wildtype mice are clearly separated by the PCA in all subsets, except in the two dopaminergic neuron types (clusters 4 and 5).

Correlation analysis on pseudo-bulk data from each subcluster revealed that gene expression changes induced by poly-GA were generally positively correlated across all cell types, especially among the neuronal subtypes (Fig. S8). CD treatment partially reversed these effects, as indicated by the negative correlation, with the most substantial impact on the *Oligo_mat1* and *Oligo_mat2* populations and neuroblasts. Moreover, filtering all poly-GA upregulated genes that were significantly rescued by CD treatment (e.g., *Neat1*, *ApoD*, *Plin4*, *Rhoj*) and plotting the UMAP highlights oligodendrocytes as the main target of CD (Fig. 2e). A similar analysis of all poly-GA downregulated genes that are rescued by CD (e.g., *Cntnap5a/b*, *Zbtb20*, *Plxn2*, *Sema5a*) showed a strong enrichment in neuroblasts average expression (Fig. 2f). Importantly, CD treatment also significantly reduced the cholesterol dysfunction in oligodendrocytes based on cell type-specific analysis of that pathway (Fig. S9). Interestingly, cholesterol export and storage pathways were mostly induced in oligodendrocytes of GA-Nes mice and less consistently in microglia and astrocytes.

Taken together, poly-GA expression induces a pronounced microgliosis in GA-Nes mice, but also affects all other cell types. CD treatment most strongly affects gene expression in oligodendrocytes and neuroblasts in transgenic mice, but has little effect in controls (Fig. S7). Since the high density of neuroblast in young GA-Nes mice is unlikely to reflect ALS/FTD pathology in aged patients, we focused our further analysis on oligodendrocytes.

CD ameliorates DOL formation in GA-Nes mice

Disease-associated oligodendrocytes (DOLs) with a common gene expression signature have recently been identified in mouse models of Alzheimer's disease, demyelination, and aging¹⁴. *Serpina3n*, *C4b*, *Il33*, and other DOL marker genes were significantly upregulated in the oligodendrocyte clusters of GA-Nes mice (Figs. 3a and S10). Many of these genes were also significantly induced in previous bulk sequencing data³⁴ from hippocampus, neocortex and less severely at in the spinal cord of GA-Nes mice at the humane endpoint (Fig. 3a). Volcano plots highlight additional genes (e.g., *Kcnma1*, *Apod*, *Plin4*) that are strongly induced in GA-Nes mice and significantly rescued by CD treatment (Fig. 3b). Immunofluorescence staining and immunoblotting with *Serpina3n* further confirmed a strong induction of DOLs in GA-Nes mice, which was significantly rescued by CD treatment (Fig. 3c–e). We confirmed the rescue of *IL33* expression using an immunoassay (Fig. 3f). Enhanced expression of the chemokine *CXCL10/IP10* in GA-Nes mice was also reduced by CD treatment (Fig. S11), while other cytokines/chemokines were unaffected by CD (Fig. S11 and S12).

CD mitigates demyelination-related pathology in GA-Nes mice

To elucidate the mode of action for CD therapy in GA-Nes mice, we analyzed gene ontology terms associated with expression changes rescued by CD treatment across different cell types. Using a cutoff of

$|LFC| > 0.5$, revealed enrichment of the myelin pathway in oligodendrocytes (*Oligo_mat1*), while axon and synapse formation was stimulated in neuroblasts (Fig. 4a). The major protein components of myelin were transcriptionally downregulated in the *Oligo_mat1* and 2 populations and these changes were partially rescued by CD, particularly in the *Oligo_mat1* subpopulation. (Fig. 4b).

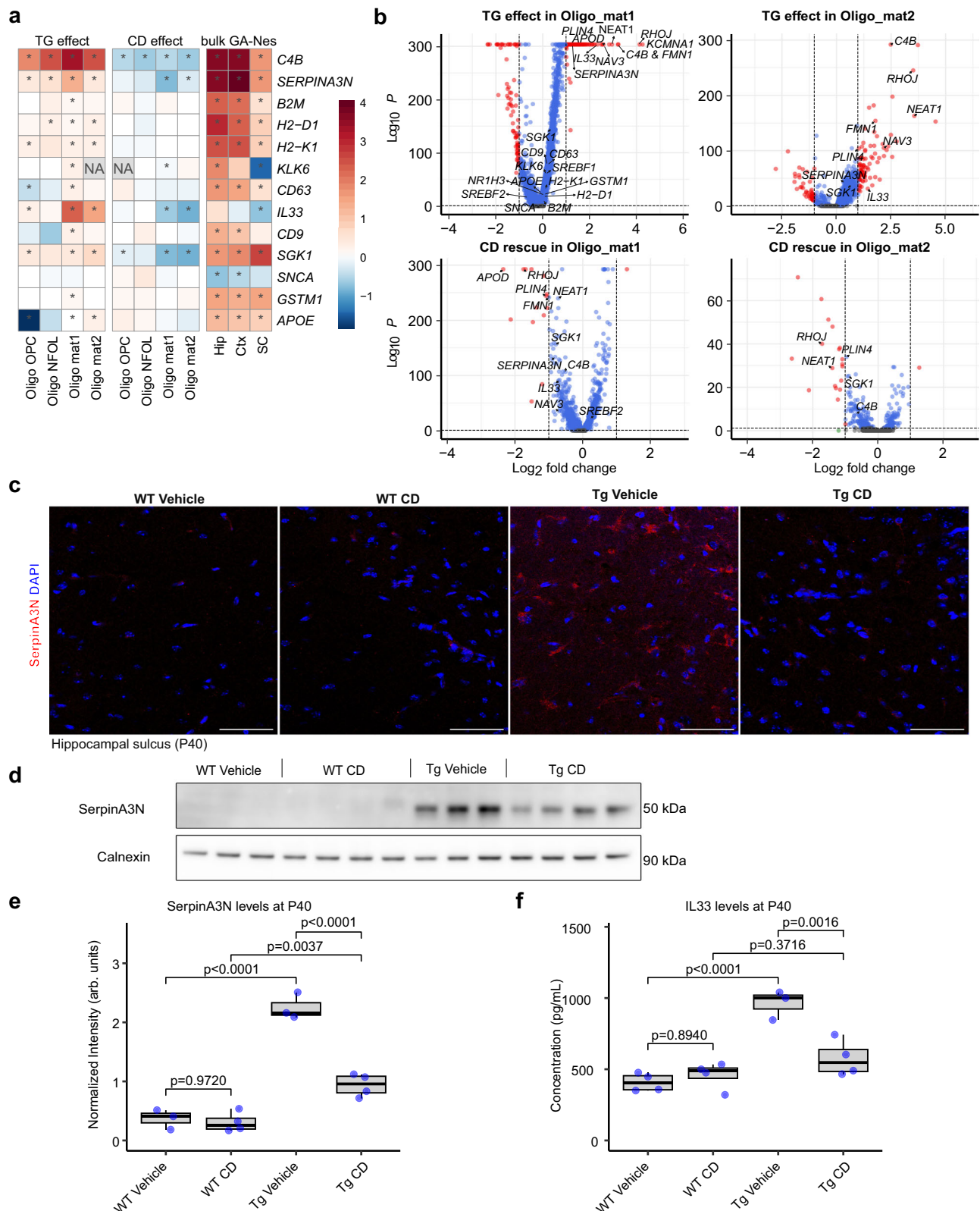
Microglia adopt different states in response to stimuli such as A β aggregates and demyelination, often termed disease-associated microglia (DAM)^{40,41}. DAM microglia, however, differ in their molecular make-up in response to different stimuli and can thus be segregated into “myelin-DAM” and “amyloid-DAM”⁴⁰. Notably, microglia in GA-Nes mice exhibited a significant upregulation of the myelin-DAM signature. Following CD treatment, this signature shifted towards amyloid-DAM, indicating a reduction in myelin debris (Fig. 4c).

To assess myelination directly, we analyzed female GA-Nes mice at P40 by electron microscopy (Fig. 4d, e). The corpus callosum was thinner, and the density of myelinated axons was greatly reduced compared to wild-type littermates. We observed some swollen axons with organelle accumulation (Fig. S13a), but large lipid droplets were absent in microglia, neurons, and oligodendrocytes. Importantly, the density of myelinated axons was significantly increased in CD-treated GA-Nes mice, suggesting that CD supports oligodendrocyte function by restoring cholesterol homeostasis (Fig. 4d, e). To distinguish between poly-GA-induced demyelination and developmentally impaired myelination, we quantified the density of myelinated axons at postnatal day 21, the time we had started CD treatment in our previous experiments. Myelination in GA-Nes mice was not significantly reduced at this young age compared to littermate controls, although there was a small trend (Fig. S13b, c), which is consistent with very modest changes at the transcriptome level at this age³⁴. This suggests that GA-Nes mice undergo active demyelination between P21 and P40, which is significantly ameliorated by CD treatment. However, since the density of myelinated axons increases significantly between P21 and P40 in wildtype mice (and to a lesser extent in transgenic mice), we cannot completely exclude the possibility of a poly-GA-dependent inhibition of developmental myelination during this period.

Given the high cholesterol content of myelin, we analyzed cholesterol and cholesterol esters by mass spectrometry. Total levels of unmodified cholesterol were decreased in GA-Nes animals compared to controls, suggesting a general loss of myelin, possibly already during development. In contrast, cholesteryl esters (especially with mono-unsaturated 18-carbon fatty acid, abbreviated as CE 18:1) were greatly increased in GA-Nes animals, with a significant rescue in CD-treated mice (Fig. 4f, g). This could reflect reduced accumulation of myelin debris, alternative metabolic processing, or excretion from the CNS.

In the absence of robust human-derived neuron/oligodendrocyte co-culture models, we overexpressed (GA)₁₄₉-GFP in iPSC-derived human neurons to investigate a potential direct effect of poly-GA on cholesterol metabolism. (GA)₁₄₉-GFP formed aggregates (Fig. S13d) similar to previous experiments in primary rat neurons⁴². Poly-GA expression resulted in a minimal but significant reduction of several cholesterol biosynthetic enzymes compared to the GFP control, without affecting lipid export or storage pathways (2.5 mg/mL from day 10 to day 19) (Fig. S13e). Interestingly, CD treatment significantly increased cholesterol biosynthetic pathways in both (GA)₁₄₉-GFP and GFP-expressing cells, suggesting that CD depletes the neuronal cholesterol pool, leading to compensatory upregulation of biosynthetic pathways. These findings are consistent with the minimal alterations in cholesterol biosynthesis, export, and storage pathways observed in neuronal populations of GA-Nes mice (see above, Fig. S9). This argues against poly-GA-induced accumulation of excess cholesterol in neurons, in contrast to the case of oligodendrocytes.

Taken together, GA-Nes mice show pronounced axon and myelin damage, evidenced by the accumulation of cholesteryl esters. CD



treatment mitigates these detrimental effects, underscoring its therapeutic potential.

Plin4 upregulation in oligodendrocytes of GA-Nes mice is rescued by CD

Among the genes rescued by CD treatment, Perilipin (Plin4) caught our attention, because it associates with lipid droplets, containing

cholesterol esters, and its expression was minimal in wild-type mice. Plin4 was strongly induced in mature oligodendrocytes of female transgenic mice, which was partially reversed by CD (Fig. 5a, b). Double immunofluorescence identified Plin4 primarily in carbonic anhydrase II (CA2)-positive oligodendrocytes of transgenic mice, with negligible expression in Iba1-positive microglia and GFAP-positive astrocytes of transgenic mice (Figs. 5c and S14). Plin4 staining was most pronounced

Fig. 3 | poly-GA transgene induces a DOL signature which is rescued by CD treatment. **a** Heatmap of previously published DOL genes⁴⁴ across oligodendrocyte clusters comparing transgenic effect ($n = 3$ Tg Vehicle vs $n = 4$ WT Vehicle) and CD effect ($n = 4$ Tg CD vs $n = 3$ Tg Vehicle) as well as bulk RNAseq from the endstage GA-Nes mice (data from³⁴, 5 control vs 5 GA-Nes mice) demonstrates induction of DOL genes in the diseased state. CD treatment showcases an appreciable and significant rescue of many of these genes. Asterisks indicate significant changes ($p < 0.05$). **b** Volcano plots of the two mature oligodendrocyte clusters demonstrate some overlap with previously published DOL genes as well as other genes such as ApoD, where they get rescued by CD treatment. **c** SerpinA3N immunofluorescence demonstrates that increased expression of this key DOL marker in transgenic GA-Nes

mice is curtailed by CD treatment, confirming the snRNAseq results. Scale bars = 50 μ m. Images are representative of two independent experiments. **d, e** Western blot of hindbrains (n from independent biological replicates: WT vehicle = 3, WT CD = 4, Tg Vehicle = 3, Tg CD = 4) and its quantification confirms the significant induction of Serpin A3N upon transgene expression and its significant rescue upon CD treatment (ANOVA, post hoc by Tukey's HSD). **f** IL33, another key DOL marker, measured by MSD V-Plex cytokine panel from hindbrain lysates shows significant modulation of this marker. Post-hoc analysis with Tukey's HSD highlights upregulation of IL33 in the transgenic condition, which is fully rescued upon CD treatment. The treatment does not modulate IL33 levels in wild-type mice. n from independent biological replicates: WT Vehicle = 4, WT CD = 4, Tg Vehicle = 3, Tg CD = 4.

in the cytoplasm of the cell body. Quantification confirmed that ~40% of CA2-positive oligodendrocytes contained Plin4 in transgenic animals, which is reduced to less than 10% in CD-treated animals matching WT expression (Fig. 5d). Taken together, poly-GA in transgenic mice induces the expression of the lipid droplet protein Plin4 predominantly in oligodendrocytes, which is partially rescued by CD treatment and may reflect cholesterol overload in the untreated GA-Nes mice.

Neuronal poly-GA and TDP-43 Δ NLS induce Plin4 expression and DOL marker expression

To exclude aberrant effects of Nestin-Cre driven poly-GA expression in oligodendrocytes, we used Camk2a-Cre to express the poly-GA transgene exclusively in excitatory neurons⁴³. These “GA-Camk2a” mice developed similar phenotypes as the GA-Nes mice, albeit at a slower pace, reaching the humane endpoint at approximately 30 weeks (Zhou et al., manuscript in preparation). In addition, we investigated the rNLS8 mouse model expressing TDP-43 Δ NLS driven by a neurofilament heavy chain promoter, resulting in almost exclusive neuronal expression and some very sparse expression in oligodendrocytes³⁶. Bulk transcriptomics analysis confirms induction of the DOL signature and cholesterol dysmetabolism, including Plin4 induction, in 30-week-old GA-Camk2a mice and 3 weeks after transgene induction in rNLS8 mice (Fig. 6a). Immunofluorescence confirmed strong induction of SerpinA3n expression in the hilus of the dentate gyrus of rNLS8 mice (Fig. 6b, c). Similarly, SerpinA3n expression was significantly induced in GA-Camk2a mice (Fig. 6d).

Finally, we confirmed the induction of Plin4 in oligodendrocytes of GA-Camk2a mice using immunofluorescence in white and gray matter of the hippocampus (Fig. 6f). In GA-Camk2a white matter, Plin4 expression was in the soma of CA2-positive oligodendrocytes (white arrow, Fig. 6f) and colocalized with the axon tracts (yellow arrow). In addition, we noticed Plin4 expression in the neuropil in white and gray matter (magenta arrow in Fig. 6f).

Taken together, Plin4 expression, DOL induction, and cholesterol dysmetabolism are conserved in a second poly-GA mouse model and a TDP-43 model with predominantly neuronal expression of aggregates.

Discussion

While ALS is not a primary demyelinating disease, significant neurodegeneration leads to myelin loss, most prominently in the corticospinal tract. Excess cholesterol from myelin loss must be stored as cholesteryl esters in the form of lipid droplets or removed from the CNS, mostly as 24S-hydroxy cholesterol^{26,44}. We explored the therapeutic potential of the cholesterol-sequestering drug CD in a C9orf72 mouse model with widespread poly-GA expression characterized by impaired cholesterol clearance and myelin loss. CD extends lifespan in female GA-Nes mice and reduces neurodegeneration markers, improves myelination, and mitigates expression of the DOL signature, including levels of the lipid droplet component Plin4. Cholesterol dysmetabolism and formation of DOLs are confirmed in a second poly-GA mouse model and a TDP-43 model with pure neuronal poly-GA expression.

Cholesterol dysmetabolism and microglia response in ALS

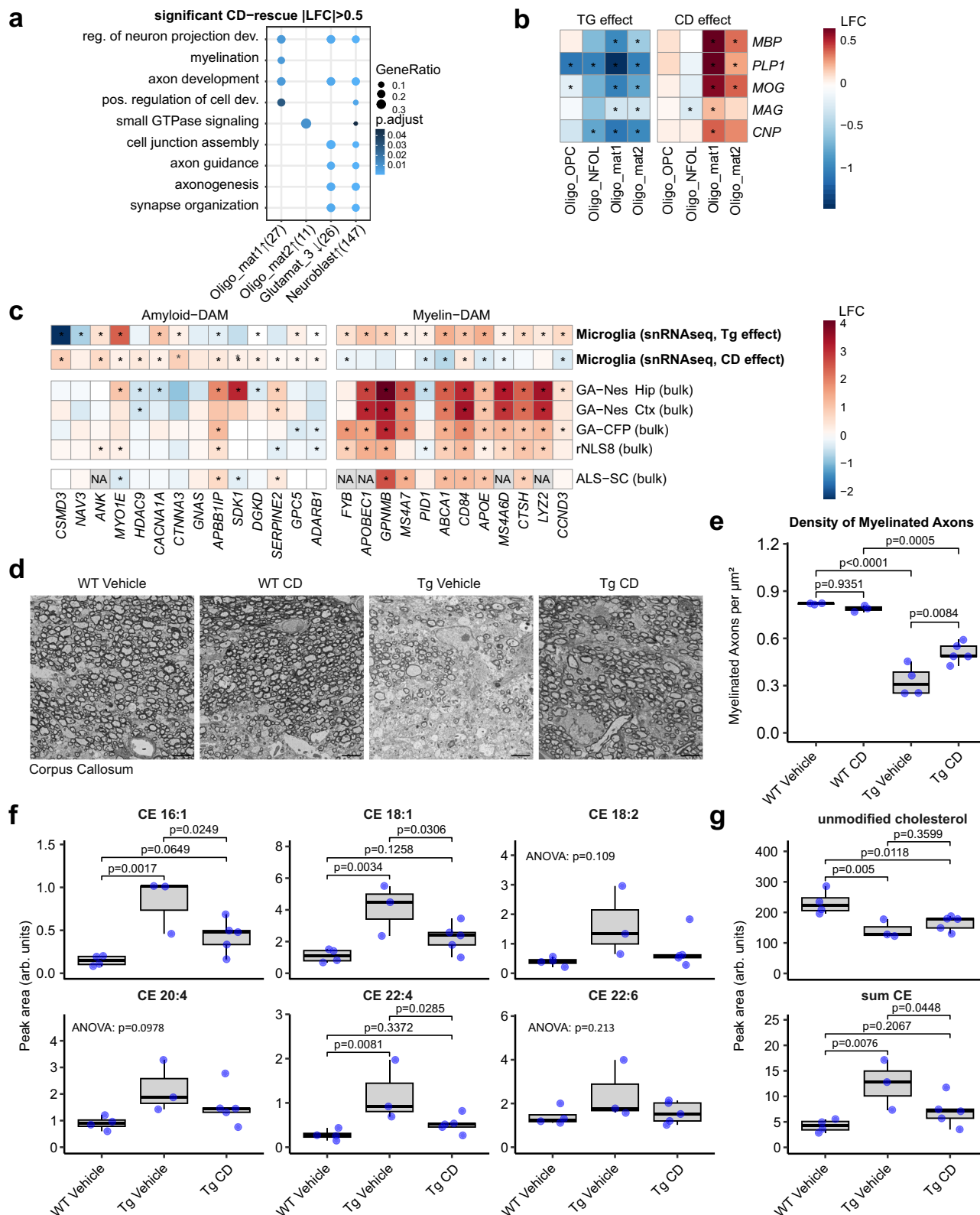
Various poly-GA and TDP-43 mouse models, along with sporadic and C9orf72 ALS patient spinal cords, show upregulation of the cholesterol export pathway (ApoE and Abca1) and a decrease in new cholesterol synthesis. This pattern resembles an LXR-driven response to an overload of toxic free cholesterol, although total cholesterol levels were even reduced in GA-Nes, which likely reflects the compromised myelination. The upregulation of C16 and C18 cholesteryl esters in GA-Nes mice strongly indicates enhanced storage of excess cholesterol in lipid droplets and aligns with findings from SOD1 mice and ALS patient tissue^{45–47}.

Cholesterol overload with subsequent LXR-response has been described in response to injury and demyelination^{23,48}. For example, induction of acute demyelination with lysolecithin in wild-type mice leads to cholesterol accumulation in microglia, resulting in a “foam cell” morphology due to uptake of cholesterol-rich myelin debris²³. As in the lysolecithin model, inefficient clearance of cholesterol may limit remyelination and thus enhance disease progression in ALS patients. Exhausting the phagocytic capacity of microglia with myelin debris has been shown to alter the microglia response towards other targets, such as A β ⁴⁰. Interestingly, the “myelin-DAM” (disease-associated microglia) signature described in demyelination models is clearly enriched in poly-GA and TDP-43 mouse models, while CD treatment reduces cholesteryl ester levels and shifts the microglia phenotype to the “amyloid-DAM” originally identified in Alzheimer's mouse model^{40,41}. Unfortunately, snRNA-seq data is less suited for subclustering of microglia than single-cell RNAseq data due to poor sensitivity for many key marker genes⁴⁹. Intracellular poly-GA and TDP-43 aggregates in ALS activate microglia, which may promote clearance or inhibit cell-to-cell transmission^{34,37,50,51}.

Excess cholesterol forms crystals that activate the inflammasome. Hydroxylated cholesterol derivatives, in particular 24S-hydroxy cholesterol, can be excreted from the CNS, but in case of clearance failure, can also be toxic to oligodendrocytes at high concentrations^{44,52}. Moreover, auto-oxidized cholesterol derivatives that harm motoneuron health have been identified in SOD1 models and ALS tissue⁵³. Although cholesteryl esters are generally inert, the acyl group donors needed for their synthesis, like phosphatidylcholine, can convert into toxic byproducts, such as lysolecithin⁴⁶. CD may inhibit all these pathways by sequestration of cholesterol, resulting in reduced DOL formation and altered microglial phenotype, suggesting therapeutic potential in modulating cholesterol-induced pathology. Interestingly, CD leads to compensatory induction of cholesterol biosynthesis and cholesterol uptake in control iPSC-derived neurons confirming the cholesterol clearance function of CD.

Lipid droplets and Plin4 in ALS

PLIN4 is a poorly characterized member of the perilipin family. It preferentially binds to cholesteryl esters and is expressed mainly in adipose tissue and muscle under physiological conditions⁵⁴. Interestingly, pathogenic mutations in Plin4 can trigger its aggregation in



muscle, resulting in a myopathy⁵⁵. Perilipins, including PLIN4, coat lipid droplets and regulate their decomposition through lipases and lysosomes⁵⁶. Moreover, PLIN4 droplets have been observed in neurons and astrocytes in Parkinson's disease mouse model induced by MPP⁺⁵⁷. The knockdown of Plin4 in SH-SY5Y cells mitigates MPP⁺ toxicity by resorting mitophagy, suggesting lipid droplets overwhelm the autophagy machinery.

In the context of ALS, Plin4 upregulation has only been reported in SOD1^{G93A} mice, where it starts before symptom onset and continues to increase to the late stage⁵⁸. However, Plin4 is predominantly expressed in neurons in the SOD1^{G93A} mice, while it is primarily expressed in oligodendrocytes in GA-Nes and GA-Camk2a mice. In addition, PLIN4 expression in oligodendrocytes has been reported in the experimental autoimmune encephalomyelitis mouse model¹⁸,

Fig. 4 | CD mitigates demyelination-related pathology in GA-Nes mice. **a** Gene ontology of genes rescued by CD with $|LFC| > 0.5$ shows that upregulated genes in Oligo_mat1 and neuroblast cluster are contributing to myelination and axonal development. The number of genes per cell type is indicated in parenthesis. **b** Heatmap of gene expression of major myelin protein components demonstrates downregulation of myelination in all oligodendrocyte clusters as the result of transgene expression (left block), an effect which is significantly rescued with CD treatment (right block). Asterisks indicate significant changes (adjusted $p < 0.05$). **c** A myelin DAM signature is detected in various models of ALS as well as patient spinal cord. Microglia cluster also strongly shows this signature, while CD administration partially alleviates this signature, shifting it more towards the amyloid DAM signature. Asterisks indicate significant changes (adjusted $p < 0.05$). **d, e** SEM overview and quantification of corpus callosum shows dramatic loss of myelinated

axons upon transgene expression, which is partially but significantly rescued by CD treatment (ANOVA, post hoc by Tukey's HSD). n from independent biological replicates: WT Vehicle = 3, WT CD = 3, Tg Vehicle = 4, Tg CD = 5. Scale bars = 3 μ m. **f** Measurements of cholesteryl ester species by mass spectrometry demonstrate significant upregulation in transgenic condition and CD-mediated rescue of CE 16:1, CE 18:1, and CE 22:4. CE 18:2, CE 20:4, and CE 22:6 were not significantly modulated (ANOVA with Fisher's LSD post-hoc). n from independent biological replicates: WT Vehicle = 4, Tg Vehicle = 3, Tg CD = 5. **g** Total unmodified cholesterol and cholesteryl esters (from peak area sum) confirm downregulation of cholesterol in transgenic condition, which is not affected by CD. Cholesteryl esters are upregulated in GA-Nes mice, which is rescued by CD (ANOVA with Fisher's LSD post-hoc). n from independent biological replicates: WT Vehicle = 4, Tg Vehicle = 3, Tg CD = 5).

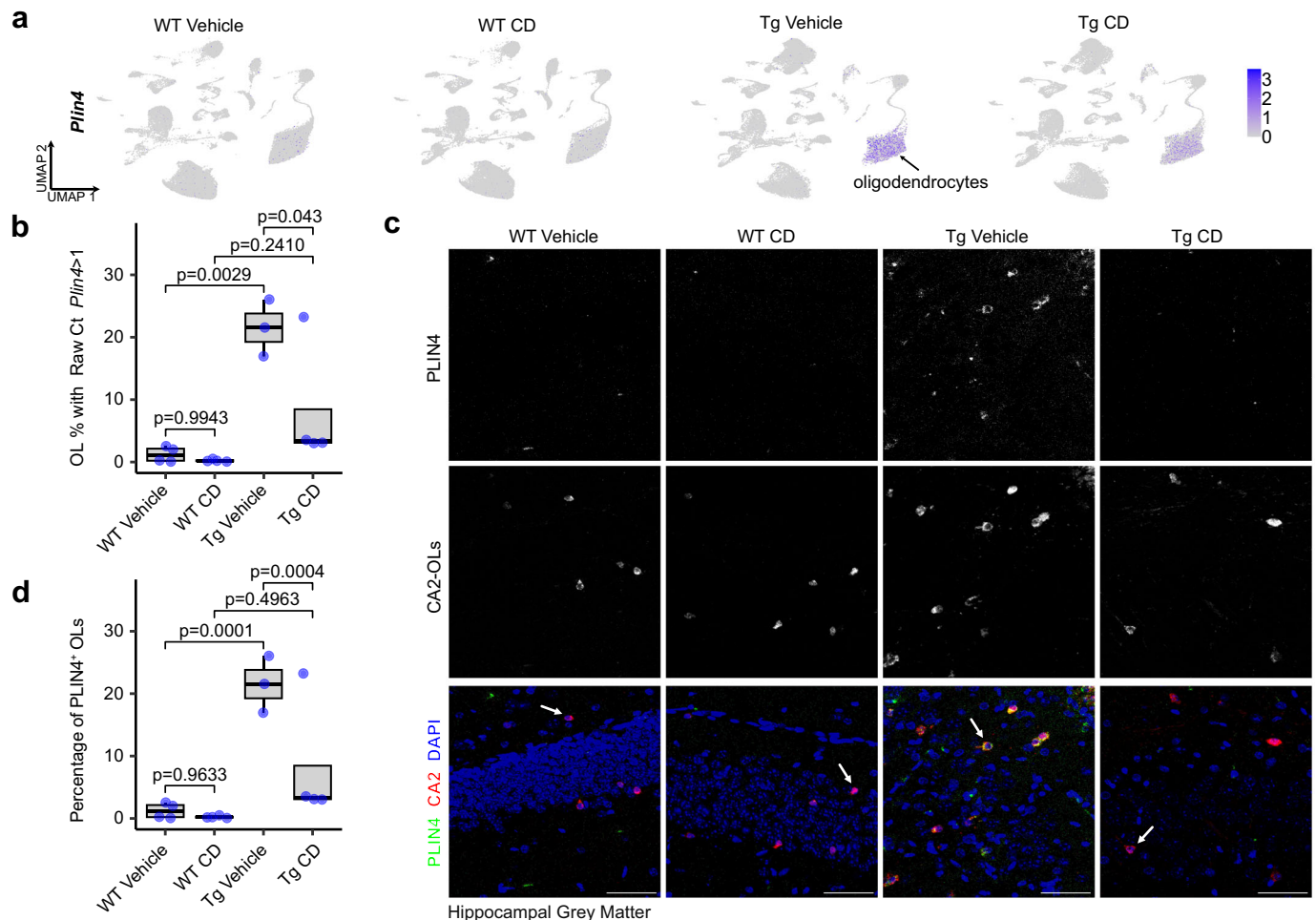


Fig. 5 | Plin4 production is upregulated in oligodendrocytes, and rescued by CD treatment. **a** FeaturePlot of PLIN4 shows upregulation of its expression in GA-Nes mice and rescue by CD treatment. Major glia types are clustered as indicated. **b** Percentage of mature oligodendrocytes expressing more than one copy of PLIN4 (raw count) is dramatically increased with the expression of the GA transgene, and partially rescued by CD treatment. Data is generated per each animal from the snRNAseq data (ANOVA, post hoc by Tukey's HSD; $n = 4$ WT Vehicle, $n = 3$ WT CD, $n = 3$ Tg Vehicle, $n = 4$ Tg CD). **c** PLIN4 (green) immunofluorescence co-stained with DAPI

and CA2 (red) confirm the transgenic upregulation and rescue by CD. White arrows indicate examples of CA2+ oligodendrocytes. Scale bars = 50 μ m; Shown images are adjusted for brightness and contrast in the same way for each channel across all conditions. **d** Quantification of percentage of PLIN4+ oligodendrocytes in hippocampus highlights a dramatic increase of such oligodendrocytes with the expression of the transgene, and a near-complete rescue by CD treatment. $n = 3$ in each of the four conditions, from independent biological replicates (ANOVA, post hoc by Tukey's HSD). Quantification was performed exclusively on raw images.

mirroring the subcellular distribution pattern we observed. These findings, together with our data, support a potential role for Plin4 in primary and secondary demyelinating diseases.

Despite strong upregulation of Plin4, we and others have not observed large lipid droplets in oligodendrocytes under demyelinating conditions. To date, lipid droplets, in this case labeled by Plin1, have

only been reported in oligodendrocytes expressing the AD risk allele ApoE4, which is mitigated by CD treatment in both cellular and animal models¹⁵. Although we did not observe cholesterol crystals or excessive lipid droplets in microglia or oligodendrocytes through (electron) microscopy, lipidomic analysis confirms a strong increase in cholesteryl esters in GA-Nes mice, which is normalized by CD treatment.

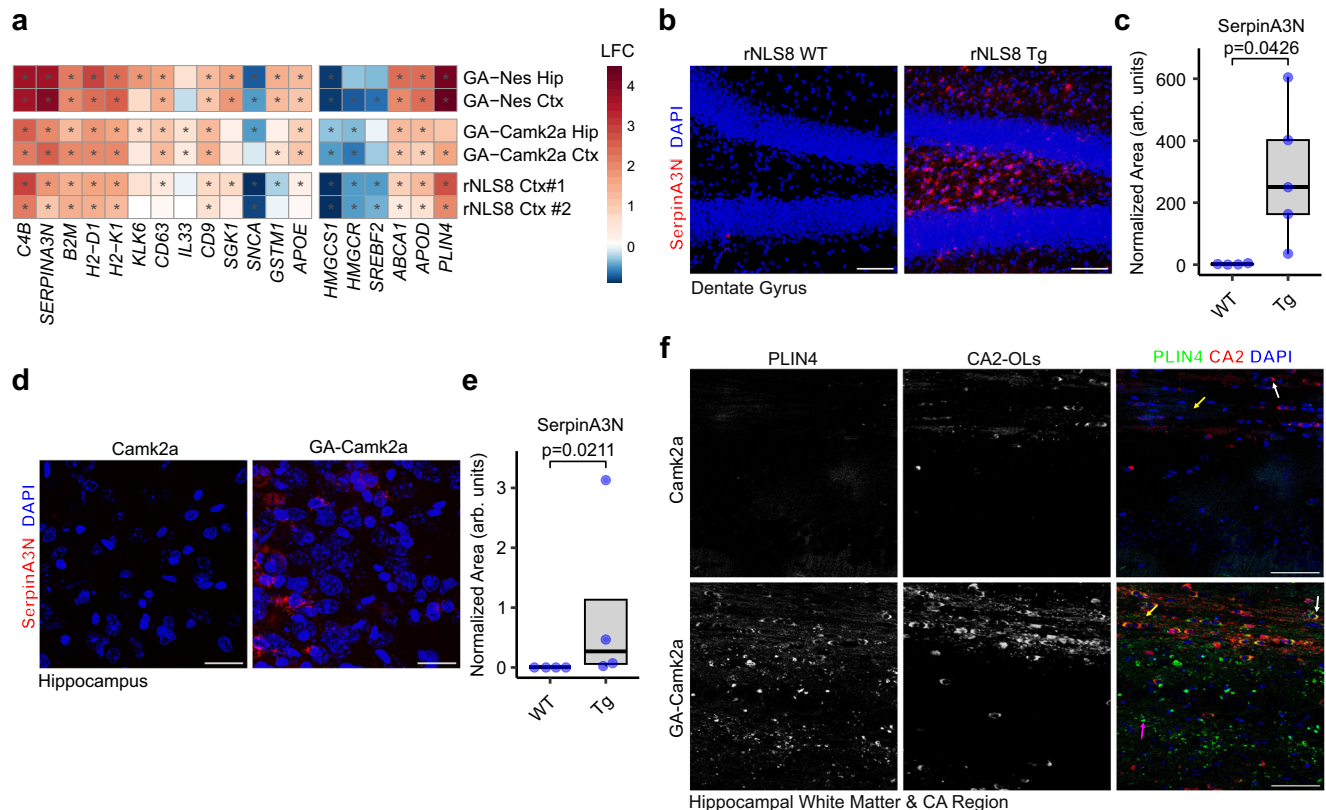


Fig. 6 | DOLs are found in other ALS mouse models. a Heatmap of DOL marker genes and essential cholesterol pathway genes from bulk RNAseq across three mouse models of ALS confirms induction of DOLs and the disturbance of cholesterol pathway. Asterisks indicate significant changes (adjusted $p < 0.05$). (n as Fig. 1a for GA-Nes and rNLS8 mice. GA-Camk2a hippocampi from 5 control vs 6 transgenic mice. GA-Camk2a neocortex from 4 control vs 6 transgenic mice). **b, c** SerpinA3N staining in rNLS mice shows significant expression of SerpinA3N mRNA in the transgenic condition. n: WT = 4, Tg = 5 from independent biological replicates. (Welch's T -test) **d, e** SerpinA3N staining in GA-Camk2a mice shows significant expression of SerpinA3N mRNA in the transgenic condition. n: WT = 4, Tg = 4 from

independent biological replicates (Mann–Whitney U -Test). **f** PLIN4 (green) immunofluorescence co-stained with DAPI and oligodendrocyte marker CA2 (red) in Camk2a (control) and GA-Camk2a (transgenic) mice, respectively, confirms upregulation of PLIN4 in transgenic mice, both in oligodendrocytes as well as elsewhere. The shown images are adjusted for brightness and contrast in the same way for each channel in similar ways across both conditions. White arrow indicates an example of a CA2+ oligodendrocyte, yellow arrow shows an example of axon tracts, while magenta arrow highlights an example of PLIN4 in the neuropil. Images are representative of three animals. Scale bar = 50 μ m.

DOLs and Oligodendrocyte dysfunction in ALS

The fascinating discovery of a conserved signature of DOLs in mouse models of Alzheimer's disease and multiple sclerosis has sparked a new interest in oligodendrocyte biology in other neurodegenerative diseases and mouse models^{14,18,19}. It is unclear whether DOLs promote neurodegeneration or reflect a protective response.

Emerging single-nucleus RNAseq data from ALS patients show that the expression of myelin-encoding genes is reduced in oligodendrocytes in the frontal cortex of C9orf72 FTD/ALS and the motor cortex of ALS cases^{59,60}, and myelination deficits have been reported^{61,62}. In addition, oligodendrocyte deficits have been documented in several ALS mouse models, including SOD1 transgenic mice¹³, FUS knockout mice⁶³, and TDP-43 knockout mice⁶⁴. A very recent study reported reduced myelination and cholesterol biosynthesis upon oligodendrocyte-specific expression of mutant TDP-43 M337V in mice, but DOL formation was not investigated¹⁷. TDP-43 aggregates are also common in oligodendrocytes, particularly in C9orf72 ALS^{4,5}, and C9orf72 and SOD1 mutations also have direct effects on oligodendrocytes that may harm motor neurons by promoting lactate release⁶⁵. Interestingly, while DPR aggregates have so far only been detected in neurons and ependymal cells, C9orf72 is also widely expressed in glial cells including oligodendrocytes^{7,8,66,67}.

The exact pathway of DOL induction is still unclear, but may involve inflammatory pathways such as STAT and NF κ B in myelinating oligodendrocytes¹⁴. GA-Nes mice show a robust DOL signature in

snRNAseq data, with several established markers verified at the protein level. In our initial characterization of the GA-Nes line using anti-GA immunohistochemistry, we mainly detected poly-GA aggregates in neurons³⁴. GFP fluorescence from cryosections revealed a more widespread expression of GFP-(GA)₁₇₅ in oligodendrocytes and astrocytes, which is consistent with the expression of Nestin-Cre also in glial progenitor cells. GA-Camk2a mice, which express poly-GA exclusively in excitatory neurons⁴³ and rNLS8 mice, with neuronal TDP-43 Δ NLS expression, also express key DOL markers, hinting at a non-cell-autonomous induction mechanism. However, given the significant expression of poly-GA in oligodendrocytes in the GA-Nes mice used for most of this study, additional cell-autonomous effects are likely in this model.

Single-cell RNAseq analysis of treated GA-Nes mice suggests that cyclodextrin mainly rescues transgene-induced gene expression changes in oligodendrocytes, including cholesterol dysmetabolism, suggesting DOL conversion may depend on cholesterol or its derivatives. This parallels findings in cancer research, where lipid droplets have been implicated in inflammation and progression through eicosanoid signaling⁶⁸. Interestingly, snRNAseq also shows strong upregulation of ApoD and the corresponding rescue by CD in GA-Nes mice, which mainly binds eicosanoids and lipids other than cholesterol⁶⁹.

DOLs have been observed in AD patients, but to a much lesser extent than in mouse models¹⁴, possibly due to limitations in available antibodies for many secreted markers. Our findings may help to

identify DOL markers that are more widely expressed in human oligodendrocytes in neurodegeneration or demyelination.

CD as a promising candidate for the therapy of neurodegenerative diseases

CD is commonly used as an excipient in pharmaceutical formulations to enhance the solubility and entrapment of various drugs. Its potential to sequester excess cholesterol has led to preclinical and clinical studies in neurodegeneration and atherosclerosis. In female GA-Nes mice, CD reduces NfL levels and cholesterol dysmetabolism in oligodendrocytes and partially rescues demyelination or improves myelination that occurs in the corpus callosum between P21 and P40. CD is beneficial in cellular and mouse models for Niemann-Pick type C disease, which is characterized by defective cholesterol export from lysosomes due to loss of NPC1 protein^{25,70,71}. In the context of AD, CD administration has been associated with increased myelination¹⁵ and decreased A β 42 production⁷². In a mouse model of stroke, CD reduced the chronic inflammation and secondary neurodegeneration, thereby averting post-stroke cognitive decline⁷³.

Despite initial approval of compassionate use in selected NPC cases, the original CD formulation adobetadex was later discontinued due to a negative risk/benefit ratio and lack of effect on Neurofilament light chain levels in the CSF⁷⁴. However, a new CD formulation (Trappsol Cyclo) is currently tested in clinical trials for NPC and AD, with promising upregulation of several hydroxylated cholesterol species and reduction of Tau CSF levels as neurodegeneration marker in NPC patients⁷⁵. Interestingly, NPC1 is essential for oligodendrocyte differentiation, and CD treatment partially restores myelination in NPC1 knockout mice⁷⁶. While we detected consistent benefits in a *C9orf72* ALS model with daily CD treatment, weekly dosing had no obvious benefits in SOD1 ALS mice⁷⁷. In addition, many biological studies using CD often do not report the degree of substitution of CD, although it greatly affects its colligative properties⁷⁸, and this could significantly affect treatment outcomes. Our gender-specific responses are consistent with data in NPC mice, although the mechanism remains elusive³⁹. Interestingly, cholesterol dysmetabolism is more pronounced in male ALS patients, and testosterone affects myelination in mice³⁸. The promyelinating effects of testosterone and differential cholesterol metabolism between the two genders may explain the dichotomy we observed in response to CD treatment, although further studies are needed.

Overall, our research underscores the significance of cholesterol dysmetabolism in *C9orf72* ALS and suggests that alleviating CNS cholesterol overload could be a viable therapeutic strategy.

Methods

Animal experiments

All animal experiments were conducted in accordance with the German Animal Welfare Law and received approval from the Government of Upper Bavaria (licenses TV 55.2-2532. Vet_02-17-106 and TV 55.2-2532. Vet_03-17-68). All mice were housed in our pathogen-free animal facility in standard cages under a 12-h light/dark cycle with ad libitum access to water and food. Breeding and genotyping schemes of GA-Nes and GA-Camk2a mice followed those outlined in our previous publication³⁴. The lines were maintained in a C57BL/6J background. The monogenic lines B6;C3-Tg(NEFH-tTA)8Vle/J (NEFH-tTA line 8, stock #025397) and B6;C3-Tg(tetO-TARDBP*)4Vle/J (tetO-hTDP-43 Δ NLS line 4, stock #014650) were obtained from the Jackson Laboratory (Bar Harbor, USA), backcrossed to C57BL/6J background, and intercrossed to generate bigenic regulatable NLS8 (rNLS8) animals³⁶. Breeders as well as offspring mice were kept on a doxycycline diet (200 mg/kg, Ssniff, Germany) until the transgene was switched to standard chow lacking doxycycline (Ssniff, Germany).

For all symptomatic lines, mashed wet chow was provided on a petri dish on the cage floor, while the animals also had ad libitum access to normal food and water. Animals were scored daily during the experiment and were monitored for weight, basic awareness and neurological condition, agility, general well-being, and wound healing. While any of these criteria could necessitate euthanasia, GA-Nes mice reached their humane endpoint mainly due to 20% weight loss. Based on the uniform transgene expression, we used multiple brain regions for analysis to adhere to the 3R principles.

(2-Hydroxypropyl)- β -cyclodextrin (CAS #128446-35-5, here referred to as CD, Sigma-Aldrich H107-100G, Degree of Substitution = 5) was dissolved in 30 mM citric buffer (pH 5.0) in normal saline (vehicle) to achieve a 20% concentration. Starting from P21, all mice received daily subcutaneous injections of 2 g/kg CD solution or an equivalent volume of the vehicle. Mice in the survival cohort were treated until they reached the humane endpoint, whereas those in the fixed cohort were harvested at P40. Survival results were analyzed by R version 4.3 and survminer package version 0.4.9 (<https://cran.r-project.org/web/packages/survminer/index.html>).

Prior to tissue collection, intracardiac blood was collected and centrifuged at 2500 $\times g$ for 10 min at 4 °C to isolate serum. Animals were perfused with ice-cold PBS prior to brain dissection, where one hemisphere was snap-frozen for biochemical investigation and the other prepared for immunohistochemistry.

GA-Nes mice in the survival experiment (both genders) were obtained from 17 litters, while the P40 cohort (only females were analyzed) was obtained from 30 litters. RNLS8 mice were obtained from three litters, while GA-Camk2a mice were obtained from two litters.

Electron microscopy

Following perfusion and immersion fixation in 2.5% GA, 4% PFA, and 2 mM CaCl₂ buffered in 0.1 M sodium cacodylate at pH 7.4 for 12 h, samples were stored for 3 days in 0.1 M sodium cacodylate buffer. Prior to further processing, 1 \times 1 mm² pieces of the hippocampus were dissected from coronal sections with fine scalpels.

Heavy metal staining, dehydration, and resin infiltration were performed following a standard reduced osmium-thiocarbohydrazide-osmium (ROTO) en bloc staining protocol⁷⁹.

EM images were obtained on a Zeiss Crossbeam Gemini 340 SEM with a four-quadrant backscattered electron detector at 8 kV. After low-resolution imaging (9500 nm pixel size) to locate the sections, regions of interest were located at intermediate resolution (ranging from 50 to 200 nm/pixel). Regions of interest were acquired at 4 nm/pixel.

Immunostaining

Paraffin sections were deparaffinized and rehydrated with xylene/alcohol washes. Heat-Induced Epitope Retrieval was performed in citrate buffer (pH 6) in a steam cooker. Frozen sections were brought to room temperature and subsequently rehydrated in PBS. For CA2+ oligodendrocyte staining in frozen sections, antigen retrieval was performed in citrate buffer (pH 6) at 80 °C. When using mouse IgG primary antibodies, ReadyProbes Mouse on Mouse IgG blocking solution (Invitrogen, R37621) was used, according to the manufacturer's specification. Subsequently, the sections were blocked and permeabilized with 5% FBS and 0.1% Triton-X-100 for 1 h at room temperature. Primary antibodies were prepared in blocking solution (2% FBS, 2% BSA, and 0.2% fish gelatin in PBS). Upon applying the primary antibody solution, slides were incubated in a humid chamber overnight at 4 °C, followed by two 5-minute washes in PBST (0.05% Tween-20 in PBS) and a final wash in PBS on the following day. After incubation of secondary antibodies for 1 h at room temperature, slides were washed as described before. Subsequently, the sections would be

incubated in a DAPI (4',6-Diamidino-2-Phenylindole, Dihydrochloride, Invitrogen, D1306) solution for 20 min, followed by two PBS washes (5 min). Lastly, sections were coverslipped (No. 1.5H, $170 \pm 5 \mu\text{m}$) with ProLong Diamond Antifade Mountant (Invitrogen, P36970).

The following primary antibodies were used: Serpin A3N (R&D Systems, AF4709, 1:200), PLIN4 (Novus Bio, NBP2-13776, 1:200), GFAP (SySy, 173 006, 1:500), IBA1 (Abcam, ab283346, 1:400; and Fujifilm Wako, 019-19741, 1:500), CA2 (R&D Systems, MAB2184, 1:200), S100B (NovusBio, NB110-57478, 1:200), Dcx (Proteintech, 13925-1-AP, 1:100), NeuN (Abcam, AB104224, 1:200).

The following secondary antibodies were used: goat anti-chicken Alexa Fluor 647 (Invitrogen, A21449, 1:250), donkey anti-goat Alexa Fluor Plus 488 (Invitrogen, A32814, 1:250), donkey anti-goat Alex Fluor Plus 555 (Invitrogen, A32816, 1:250), donkey anti-rabbit Alex Fluor Plus 555 (Invitrogen, A32794, 1:250), goat anti-rat Alexa Fluor 647 (Invitrogen, A-21247, 1:250), donkey anti-mouse Alexa Fluor Plus 647 (Invitrogen, A32787, 1:250).

Microscopy and image analysis

All fluorescence microscopy images in this study were captured using a Zeiss LSM710 confocal laser scanning microscope with ZEN 2010 software. Brightfield images were obtained with Leica DMi8 inverted microscope. To analyze images, Python 3.8 was used with the following packages: aicsimageio version 4.9.4 (<https://github.com/AllenCellModeling/aicsimageio>), numpy version 1.23.5⁸⁰, opencv-python version 4.6.0⁸¹, scikit-image version 0.19.3⁸², Cellpose⁸³, and pandas version 2.0.3. CZI files were read into Python using the AICSImageio library. Cellpose models were used to quantify cell count in confocal images as well as the number of myelinated axons in EM images. For Z-stacks, every z-plane was analyzed separately, and the results were averaged. To assess the staining area, images were thresholded (manually or with threshold_li from scikit-image, as appropriate). Further background areas consisting of very small noise were also removed using a size filter (scikit-image). Colocalization was assessed using numpy array overlap and labeled using scikit-image. The results of the analyses were plotted with the ggplot2 library version 3.5.1 in R version 4.4.1.

Immunoblotting

To extract proteins from tissue, frozen hindbrains were pulverized with a pestle and mortar. RIPA buffer (Serva, 39244.01) supplemented with 2% sodium dodecyl sulfate (SDS) and Halt protease inhibitor cocktail (Thermo Scientific, 78429) was added. Homogenization was done in Percellys 2 mL soft tissue tubes (Bertin Corp., P000912-LYSKO-A) with the Percellys homogenizer at 4 °C. Protein concentration was determined with BCA assay (Thermo Scientific, 23225).

For immunoblotting, Novex 10–20% Tricine gels (Invitrogen, EC66252BOX) were loaded with 20 μg of protein per well. Transfer was done using iBlot2® PVDF mini stacks (Invitrogen, IB24002) on an iBlot2 gel transfer device (Invitrogen, IB21001) using the default PO program. Membranes were blocked with 0.2% iBlock (Invitrogen, T2015) in TBS Triton-X-100 for 1 h at room temperature, while shaking. Serpin A3N (R&D Systems, AF4709; 1:2000) and Calnexin (Enzo, ADI-SPA-860-F; 1:7000) antibodies and their respective anti-goat HRP and anti-rabbit HRP conjugated antibodies (1:5000) were used for western blotting. HRP-bound proteins were detected with Immobilon Forte Western HRP substrate (Millipore, WBLUF0500) using cytiva's Amersham ImageQuant 800 device.

Immunoassays

To perform MSD immunoassays, V-PLEX Proinflammatory Panel 1 Mouse kit (MSD, K15048D-2) and V-PLEX Cytokine Panel 1 Mouse kit (MSD, K15245D-2) were used on hindbrain lysates. For the proinflammatory panel, 13 mg/mL of protein per well was taken, while 5 mg/mL of protein per well was needed for the cytokine panel. The assay was performed according to the manufacturer's protocol, and the

plates were read with MSD's MESO QuickFlex SQ 120MM plate reader. Concentrations of the biomarkers were calculated in manufacturer's software, and the exported values within detection range were taken to R for visualization and statistical analysis, as described previously.

Serum NFL was measured with the NF-light Advantage Assay Kit (Quanterix, Cat. No. 103186) according to the manufacturer's protocol.

Cholesterol and cholesteryl ester measurement

Midbrain homogenates were prepared at 100 mg/mL in PBS with 20 μg /mL BHT using Precellys Ceramic Beads at 4 °C. Homogenates were stored at -80°C and then thawed to room temperature for lipid extraction. 50 μL of homogenate were transferred to glass Qsert vials containing 200 μL isopropanol with internal standards (UltimateS-plash ONE, Avanti Polar Lipids). Samples were vortexed for 10 min at room temperature and then placed at -20°C for 60 min. Samples were centrifuged for 20 min at $4000 \times g$ at 10°C . 150 μL supernatant was transferred to new glass Qsert vials. Samples were stored temporarily at -80°C , then thawed, and 75 μL were diluted with 25 μL isopropanol prior to LC-MS analysis of cholesterol and cholesteryl esters. A Waters Acquity Premier UPLC system was used to inject 5 μL onto a Thermo Scientific Accucore C30 LC column ($2.1 \times 150 \text{ mm}$, $2.6 \mu\text{m}$) at 45°C at a constant flow rate of 0.26 mL/min with initial mobile phase composition 70% A (60% acetonitrile, 40% water, 0.1% formic acid, 10 mM ammonium formate) and 30% B (88% isopropanol, 10% acetonitrile, 2% water, 0.1% formic acid, 10 mM ammonium formate). Mobile phase B was increased to 43% at 2.00 min, to 55% at 2.10 min, to 65% at 12.00 min, to 85% at 18.00 min, to 100% at 20.00 min, held at 100% for 5.00 min, then equilibrated at 30% B for 5.00 min. Full MS scans in positive polarity were acquired on Thermo Scientific Q Exactive Plus mass spectrometer, with resolution setting 70,000 (at 200 m/z), AGC target $1e6$, maximum injection time 256 ms, with scan range 365–380 m/z from 0 to 16 min and 630–780 m/z from 16 to 30 min. Peak areas for cholesterol and cholesterol esters were extracted from the raw data using Thermo Scientific Xcalibur software.

snRNAseq nuclei isolation and library preparation

Nuclei from P40 female hippocampi with acceptable RNA quality RNA Integrity Number (RIN) >7 , with Agilent RNA 6000 Nano kit (Agilent, 50671511), were isolated according to Frankenstein protocol for nuclei isolation from fresh and frozen tissue⁸⁴. Nuclei were sorted via fluorescence-activated nuclei sorting (FANS) by a DAPI+ gate and two further gates of NeuN-positive and NeuN-negative nuclei (anti-NeuN antibody from Abcam, ab190195) to obtain 5000 neurons and 5000 glia per sample, respectively.

The nuclei were processed with Chromium Next GEM Single Cell 3' Kit v3.1 (10x Genomics, 1000268) generate the cDNA libraries for this study. Gel Bead-in-Emulsions (GEMs) were generated with chip G (10x Genomics, 1000120) on the microfluidic platform 10x Genomics Chromium Single Cell Controller. Next, the samples were uniquely barcoded to distinguish the mRNAs (each having unique molecular identifier (UMI)) from different nuclei.

The cDNA was extracted with Dynabeads MyOne SILANE beads (Invitrogen, 370–12 D) and amplified by PCR. The PCR product was purified with SPRIselect reagent (Beckman Coulter, Cat #B23318). Subsequently, the 3' gene expression library was constructed with primers for Illumina NGS platform and Dual Index Kit TT set A (10x Genomics, 1000215), which allows individual sample identification.

The pooled libraries were sequenced on Illumina's NovaSeq6000 system using S4 flow cell type (500 M reads/sample) with a $2 \times 150 \text{ bp}$ paired-end read length.

snRNAseq data analysis

The raw sequencing data were initially processed using Cell Ranger software from 10x Genomics to align reads to the mouse reference

genome, followed by the creation of a Seurat object. A series of quality control measures were performed on the data where doublet score was calculated on a sample level. Then clustering was performed with high resolution, and clusters with more than 20% doublets were completely removed. Next, clusters with low-quality cells (mitochondrial gene expression, too many/few genes/UMIs) were also fully removed. Subsequently, we performed more rigorous quality control, where we deleted the individual cells with a higher-than-average doublet score or mitochondrial content using Seurat version 4.3.0⁸⁵ in R 4.2.0.

Using Seurat's built-in functions, the Seurat object was normalized by a scale factor of 10,000, and variable features were found using 3000 features with the "vst" selection method. The data was then scaled, and principal component analysis (PCA) was run on it with 25 dimensions (minimum 15 necessary as per elbow plot). Next, the data was integrated using Harmony version 0.1.1⁸⁶. The Seurat object subsequently underwent dimensionality reduction by UMAP with 45 dimensions (as informed by the elbow plot) and the reduction parameter set to 'harmony'. "FindNeighbors" function was then used to prepare the data for clustering, with 45 dimensions. To achieve optimal clustering, we tried multiple resolutions in the function "FindClusters". Based on analysis of these clusters with clustree version 0.5.0⁸⁷ and manual inspection of the UMAPs, we chose a resolution of 0.45 as the best compromise.

To annotate the clusters, "FindAllMarkers" function from Seurat was used, and the outputs were sorted. Some clusters were identified by known markers, such as GFAP, as a marker for astrocytes. For other clusters, the top markers were fed into PanglaoDB⁸⁸ to have a more informative and less biased clustering. Clusters that identified dentate gyrus (DG) neurons were identified with Janelia's Hipposeq⁸⁹ based on their top markers.

To perform pseudobulk analysis, the data were converted using SingleCellExperiment package version 1.20.0⁹⁰. The complete expression data are shown in Supplementary Data 3. Aggregated count data were fed to DESeq2 package version 1.36.0⁹¹ to obtain differentially expressed genes and generate PCA plots. All FeaturePlots and DotPlots were generated via Seurat's built-in functions.

iPSC derived neuron model

Human neurons were generated by doxycycline-mediated induction of NGN2 expression in small molecule neural precursor cells (smNPC) from a healthy female donor as previously described (GM23280, iPSC line obtained from the Coriell Institute)^{92,93}. The smNPCs are maintained in expansion medium containing N2B27 medium supplemented with CHIR99021 (StemCell Technologies, 100–1042; 3 μ M), PMA (0.5 μ M), and ascorbic acid (Sigma, A8960; 64 mg/L). For treatment, smNPCs are differentiated into iNeurons through NGN2 expression induced by doxycycline (2.5 μ g/mL). After induction, smNPCs differentiate into iNeurons within 5 days, demonstrating robust neuronal identity in this model, with MAP2 as a pan-neuronal marker and BRN2 as a marker for upper cortical layer neurons^{93,94}, which was further confirmed by transcriptomics (GEO [GSE285209](#)).

iNeurons are transduced with (GA)₁₄₉-GFP and GFP lentiviral constructs on day 7, media change to remove excess virus on day 8, and CD (2.5 mg/mL) treatments were initiated at day 10. CD was added to the media at the same concentration every other day. On day 19, RNA was isolated using Qiagen RNeasy Micro Kit according to the manufacturer's instructions. The transcriptome analysis was performed at BGI (China). After cDNA library preparation, 100 bp paired-end sequencing was performed on a DNBSQ platform at a depth of ~20 million read pairs per sample. Reads were aligned to the human genome (GRCh38.p14) at BGI, and differential gene expression was analyzed using SummarizeOverlaps and DESeq2⁹¹. The complete expression data are shown in Supplementary Data 4.

Bulk RNAseq and analysis

We reanalyzed several previously published transcriptomics datasets for GA-Nes mice³⁴, GA-CFP mice (GEO [GSE138413](#))³⁷, and rNLS8 mice (GEO [GSE233669](#))⁵¹. To replicate the GA-CFP ([GSE289729](#)) and rNLS8 ([GSE290262](#)) data, we used the control groups from ongoing treatment studies. Briefly, total RNA was extracted from mouse brain cortex with the RNeasy Plus Mini Kit (Qiagen) according to the manufacturer's instructions. Quality control was performed, and RNA samples with RIN values above 7 (Agilent) were sent to BGI Genomics (China) for transcriptome analysis. Data were aligned to the mouse genome (GRCm38), and differential gene expression was analyzed using DESeq2. For the GA-Camk2a mouse line we used Prime-seq⁹⁵ from multiple brain regions for a more extensive study. The relevant data can be found at GEO with accession [GSE291440](#). Data were aligned to the mouse genome (GRCm39), and differential gene expression was analyzed using DESeq2. For the human ALS transcriptomics data, we downloaded all publicly available RNAseq data from TargetALS (June 2024). We included all spinal cord samples from patients with ALS and controls without CNS comorbidity and with available C9orf72 genotype information. Reads were aligned to GRCh38 using STAR aligner v2.4.2a from the New York Genome Center and further processed by us using SummarizeOverlaps in R. Count tables were analyzed using DESeq2⁹¹ in a linear model adjusting the diagnosis for sex and anatomical subregions (cervical: 19 controls, 131 ALS, 28 C9orf72 ALS; thoracic: 9 controls, 46 ALS, 7 C9orf72; lumbar: 16 controls, 122 ALS, 24 C9orf72 ALS). Analyzing two subgroups (before and after June 2020) gave the same results (data not shown).

Statistics and reproducibility

Statistical analyses were performed using R version 4.3. Statistical significance was determined using Welch's *t*-test or Mann–Whitney *U*-Test for pairwise comparison or using one-way ANOVA for multiple comparisons followed by Tukey's HSD posthoc or Fisher's LSD. All analyses were two-tailed. Tukey's HSD posthoc inherently corrects for multiple comparisons. The survival curves were generated with the Survminer package in R, and the statistical comparison was conducted using Log-Rank test. Experimental group sizes (*n*) and *p* value significance levels are reported in the figures, their legends, and the Source Data file. *p* values less than 0.05 were considered to be statistically significant. In all the boxplots, the bounds of the box span from 25% to 75% percentile (first and third quartiles), and the whiskers represent the most extreme data points that are within 1.5 times the interquartile range (IQR) of those quartiles. The line in the middle of boxplots represents the median. In addition, individual data points are plotted. Source data are provided for all the underlying raw data, statistics, and blots.

After observing beneficial effects of CD in a pilot study, we generated three additional cohorts for replication and tissue collection for biochemistry, histology, and EM analysis, with reproducible results. Treatment with CD or vehicle was randomized using a random number generator. snRNAseq and its initial analysis were blinded. The genotype of GA-Nes mice could not be concealed from researchers due to obvious pathology. The subsequent wet lab experiments (e.g., staining) were effectively blinded.

Reporting summary

Further information on research design is available in the Nature Portfolio Reporting Summary linked to this article.

Data availability

Source Data is provided as a Source Data file including raw data and underlying statistical analyses of figures. SNRNAseq data can be accessed under GEO accession number [GSE262778](#). Bulk RNAseq data iPSC-derived neurons ([GSE285209](#)), GA-CFP mice ([GSE289729](#)), rNLS8

(GSE290262), and GA-Camk2a mice (GSE291440) are available at NCBI GEO. Data is available from the corresponding author upon request. Source data are provided with this paper.

References

- Hardiman, O. et al. Amyotrophic lateral sclerosis. *Nat. Rev. Dis. Prim.* **3**, 17071 (2017).
- Feldman E. L. et al. *Amyotrophic Lateral Sclerosis* (Lancet, 2022).
- Mackenzie, I. R. et al. Dipeptide repeat protein pathology in C9ORF72 mutation cases: clinico-pathological correlations. *Acta Neuropathol.* **126**, 859–879 (2013).
- Neumann, M. et al. TDP-43-positive white matter pathology in frontotemporal lobar degeneration with ubiquitin-positive inclusions. *J. Neuropathol. Exp. Neurol.* **66**, 177–183 (2007).
- Murray, M. E. et al. Clinical and neuropathologic heterogeneity of c9FTD/ALS associated with hexanucleotide repeat expansion in C9ORF72. *Acta Neuropathol.* **122**, 673–690 (2011).
- Mori, K. et al. Bidirectional transcripts of the expanded C9orf72 hexanucleotide repeat are translated into aggregating dipeptide repeat proteins. *Acta Neuropathol.* **126**, 881–893 (2013).
- Mori, K. et al. The C9orf72 GGGGCC repeat is translated into aggregating dipeptide-repeat proteins in FTL/ALS. *Science* **339**, 1335–1338 (2013).
- Ash, P. E. et al. Unconventional translation of C9ORF72 GGGGCC expansion generates insoluble polypeptides specific to c9FTD/ALS. *Neuron* **77**, 639–646 (2013).
- Gendron, T. F. et al. Antisense transcripts of the expanded C9ORF72 hexanucleotide repeat form nuclear RNA foci and undergo repeat-associated non-ATG translation in c9FTD/ALS. *Acta Neuropathol.* **126**, 829–844 (2013).
- Zu, T. et al. RAN proteins and RNA foci from antisense transcripts in C9ORF72 ALS and frontotemporal dementia. *Proc. Natl. Acad. Sci. USA* **110**, E4968–E4977 (2013).
- Khosravi, B. et al. Cell-to-cell transmission of C9orf72 poly-(Gly-Ala) triggers key features of ALS/FTD. *EMBO J.* **39**, e102811 (2020).
- Northall, A. et al. Multimodal layer modelling reveals in vivo pathology in amyotrophic lateral sclerosis. *Brain* **147**, 1087–1099 (2024).
- Kang, S. H. et al. Degeneration and impaired regeneration of gray matter oligodendrocytes in amyotrophic lateral sclerosis. *Nat. Neurosci.* **16**, 571–579 (2013).
- Kenigsbuch, M. et al. A shared disease-associated oligodendrocyte signature among multiple CNS pathologies. *Nat. Neurosci.* **25**, 876–886 (2022).
- Blanchard, J. W. et al. APOE4 impairs myelination via cholesterol dysregulation in oligodendrocytes. *Nature* **611**, 769–779 (2022).
- Chen, W. T. et al. Spatial transcriptomics and in situ sequencing to study Alzheimer's disease. *Cell* **182**, 976–991 e919 (2020).
- Horiuchi, M. et al. ALS-linked mutant TDP-43 in oligodendrocytes induces oligodendrocyte damage and exacerbates motor dysfunction in mice. *Acta Neuropathol. Commun.* **12**, 184 (2024).
- Falcao, A. M. et al. Disease-specific oligodendrocyte lineage cells arise in multiple sclerosis. *Nat. Med.* **24**, 1837–1844 (2018).
- Pandey, S. et al. Disease-associated oligodendrocyte responses across neurodegenerative diseases. *Cell Rep.* **40**, 111189 (2022).
- Zhou, Y. et al. Human and mouse single-nucleus transcriptomics reveal TREM2-dependent and TREM2-independent cellular responses in Alzheimer's disease. *Nat. Med.* **26**, 131–142 (2020).
- Kaya, T. et al. CD8(+) T cells induce interferon-responsive oligodendrocytes and microglia in white matter aging. *Nat. Neurosci.* **25**, 1446–1457 (2022).
- Stadelmann, C., Timmler, S., Barrantes-Freer, A. & Simons, M. Myelin in the central nervous system: structure, function, and pathology. *Physiol. Rev.* **99**, 1381–1431 (2019).
- Cantuti-Castelvetri, L. et al. Defective cholesterol clearance limits remyelination in the aged central nervous system. *Science* **359**, 684–688 (2018).
- Zimmer, S. et al. Cyclodextrin promotes atherosclerosis regression via macrophage reprogramming. *Sci. Transl. Med.* **8**, 333ra350 (2016).
- Tanaka, Y. et al. Efficacy of 2-hydroxypropyl-beta-cyclodextrin in Niemann-Pick disease Type C model mice and its pharmacokinetic analysis in a patient with the disease. *Biol. Pharm. Bull.* **38**, 844–851 (2015).
- Hartmann, H., Ho, W. Y., Chang, J. C. & Ling, S. C. Cholesterol dyshomeostasis in amyotrophic lateral sclerosis: cause, consequence, or epiphenomenon? *FEBS J.* **289**, 7688–7709 (2022).
- Mariosa, D. et al. Blood biomarkers of carbohydrate, lipid, and apolipoprotein metabolisms and risk of amyotrophic lateral sclerosis: a more than 20-year follow-up of the Swedish AMORIS cohort. *Ann. Neurol.* **81**, 718–728 (2017).
- Thompson, A. G., Talbot, K. & Turner, M. R. Higher blood high density lipoprotein and apolipoprotein A1 levels are associated with reduced risk of developing amyotrophic lateral sclerosis. *J. Neurol. Neurosurg. Psychiatry* **93**, 75–81 (2022).
- Dupuis, L. et al. Dyslipidemia is a protective factor in amyotrophic lateral sclerosis. *Neurology* **70**, 1004–1009 (2008).
- Peter, R. S. et al. Life course body mass index and risk and prognosis of amyotrophic lateral sclerosis: results from the ALS registry Swabia. *Eur. J. Epidemiol.* **32**, 901–908 (2017).
- Dupuis, L., Pradat, P. F., Ludolph, A. C. & Loeffler, J. P. Energy metabolism in amyotrophic lateral sclerosis. *Lancet Neurol.* **10**, 75–82 (2011).
- Diekstra, F. P. et al. Mapping of gene expression reveals CYP27A1 as a susceptibility gene for sporadic ALS. *PLoS ONE* **7**, e35333 (2012).
- van Rheenen, W. et al. Common and rare variant association analyses in amyotrophic lateral sclerosis identify 15 risk loci with distinct genetic architectures and neuron-specific biology. *Nat. Genet.* **53**, 1636–1648 (2021).
- LaClair, K. D. et al. Congenic expression of poly-GA but not poly-PR in mice triggers selective neuron loss and interferon responses found in C9orf72 ALS. *Acta Neuropathol.* **140**, 121–142 (2020).
- Schludi, M. H. et al. Spinal poly-GA inclusions in a C9orf72 mouse model trigger motor deficits and inflammation without neuron loss. *Acta Neuropathol.* **134**, 241–254 (2017).
- Walker, A. K. et al. Functional recovery in new mouse models of ALS/FTLD after clearance of pathological cytoplasmic TDP-43. *Acta Neuropathol.* **130**, 643–660 (2015).
- Zhou, Q. et al. Active poly-GA vaccination prevents microglia activation and motor deficits in a C9orf72 mouse model. *EMBO Mol. Med.* **12**, e10919 (2020).
- Esperante, I. J. et al. Testosterone reduces myelin abnormalities in the wobbler mouse model of amyotrophic lateral sclerosis. *Biomolecules* **14**, 428 (2024).
- Holzmann, C., Witt, M., Rolfs, A., Antipova, V. & Wree, A. Gender-specific effects of two treatment strategies in a mouse model of Niemann-Pick disease type C1. *Int. J. Mol. Sci.* **22**, 2539 (2021).
- Depp, C. et al. Myelin dysfunction drives amyloid-beta deposition in models of Alzheimer's disease. *Nature* **618**, 349–357 (2023).
- Keren-Shaul, H. et al. A unique microglia type associated with restricting development of Alzheimer's disease. *Cell* **169**, 1276–1290.e1217 (2017).
- May, S. et al. C9orf72 FTL/ALS-associated Gly-Ala dipeptide repeat proteins cause neuronal toxicity and Unc119 sequestration. *Acta Neuropathol.* **128**, 485–503 (2014).
- Minichiello, L. et al. Essential role for TrkB receptors in hippocampus-mediated learning. *Neuron* **24**, 401–414 (1999).
- Sodero, A. O. 24S-hydroxycholesterol: cellular effects and variations in brain diseases. *J. Neurochem.* **157**, 899–918 (2021).

45. Cutler, R. G., Pedersen, W. A., Camandola, S., Rothstein, J. D. & Mattson, M. P. Evidence that accumulation of ceramides and cholesterol esters mediates oxidative stress-induced death of motor neurons in amyotrophic lateral sclerosis. *Ann. Neurol.* **52**, 448–457 (2002).
46. Dodge, J. C. et al. Neutral lipid cacostasis contributes to disease pathogenesis in amyotrophic lateral sclerosis. *J. Neurosci.* **40**, 9137–9147 (2020).
47. Chaves-Filho, A. B. et al. Alterations in lipid metabolism of spinal cord linked to amyotrophic lateral sclerosis. *Sci. Rep.* **9**, 11642 (2019).
48. Zambusi, A. et al. TDP-43 condensates and lipid droplets regulate the reactivity of microglia and regeneration after traumatic brain injury. *Nat. Neurosci.* **25**, 1608–1625 (2022).
49. Thrupp, N. et al. Single-nucleus RNA-Seq is not suitable for detection of microglial activation genes in humans. *Cell Rep.* **32**, 108189 (2020).
50. Spiller, K. J. et al. Microglia-mediated recovery from ALS-relevant motor neuron degeneration in a mouse model of TDP-43 proteinopathy. *Nat. Neurosci.* **21**, 329–340 (2018).
51. Riemenschneider, H. et al. Targeting the glycine-rich domain of TDP-43 with antibodies prevents its aggregation in vitro and reduces neurofilament levels in vivo. *Acta Neuropathol. Commun.* **11**, 112 (2023).
52. Nury, T. et al. Induction of oxipoptophagy on 158N murine oligodendrocytes treated by 7-ketocholesterol-, 7 β -hydroxycholesterol-, or 24(S)-hydroxycholesterol: protective effects of α -tocopherol and docosahexaenoic acid (DHA; C22:6 n-3). *Steroids* **99**, 194–203 (2015).
53. Dodge, J. C., Yu, J., Sardi, S. P. & Shihabuddin, L. S. Sterol auto-oxidation adversely affects human motor neuron viability and is a neuropathological feature of amyotrophic lateral sclerosis. *Sci. Rep.* **11**, 803 (2021).
54. Hsieh, K. et al. Perilipin family members preferentially sequester to either triacylglycerol-specific or cholesteryl-ester-specific intracellular lipid storage droplets. *J. Cell Sci.* **125**, 4067–4076 (2012).
55. Ruggieri, A. et al. Multiomic elucidation of a coding 99-mer repeat-expansion skeletal muscle disease. *Acta Neuropathol.* **140**, 231–235 (2020).
56. Sztalryd, C. & Brasaemle, D. L. The perilipin family of lipid droplet proteins: gatekeepers of intracellular lipolysis. *Biochim. Biophys. Acta Mol. Cell Biol. Lipids* **1862**, 1221–1232 (2017).
57. Han, X. et al. Plin4-dependent lipid droplets hamper neuronal mitophagy in the MPTP/p-Induced mouse model of Parkinson's disease. *Front. Neurosci.* **12**, 397 (2018).
58. Zhu, L. et al. Perilipin 4 protein: an impending target for amyotrophic lateral sclerosis. *Mol. Neurobiol.* **58**, 1723–1737 (2021).
59. Wang, H. V. et al. Single-nucleus multiome analysis of the prefrontal cortex from C9orf72 ALS/FTD patients illuminates pathways affected during disease progression. *bioRxiv*, (2023).
60. Limone, F. et al. Single-nucleus sequencing reveals enriched expression of genetic risk factors in extratelencephalic neurons sensitive to degeneration in ALS. *Nat. Aging* **4**, 984–997 (2024).
61. Lorente Pons, A. et al. Oligodendrocyte pathology exceeds axonal pathology in white matter in human amyotrophic lateral sclerosis. *J. Pathol.* **251**, 262–271 (2020).
62. Sirisi, S. et al. Myelin loss in C9orf72 hexanucleotide expansion carriers. *J. Neurosci. Res.* **100**, 1862–1875 (2022).
63. Guzman, K. M. et al. Conditional depletion of Fus in oligodendrocytes leads to motor hyperactivity and increased myelin deposition associated with Akt and cholesterol activation. *Glia* **68**, 2040–2056 (2020).
64. Heo, D. et al. Stage-specific control of oligodendrocyte survival and morphogenesis by TDP-43. *Elife* **11**, e75230 (2022).
65. Ferraiuolo, L. et al. Oligodendrocytes contribute to motor neuron death in ALS via SOD1-dependent mechanism. *Proc. Natl. Acad. Sci. USA* **113**, E6496–E6505 (2016).
66. Tabula Muris, C. et al. Single-cell transcriptomics of 20 mouse organs creates a Tabula Muris. *Nature* **562**, 367–372 (2018).
67. Schludi, M. H. et al. Distribution of dipeptide repeat proteins in cellular models and C9orf72 mutation cases suggests link to transcriptional silencing. *Acta Neuropathol.* **130**, 537–555 (2015).
68. Cruz, A. L. S., Barreto, E. A., Fazolini, N. P. B., Viola, J. P. B. & Bozza, P. T. Lipid droplets: platforms with multiple functions in cancer hallmarks. *Cell Death Dis.* **11**, 105 (2020).
69. Rassart, E., Desmarais, F., Najib, O., Bergeron, K. F. & Mounier, C. Apolipoprotein D. *Gene* **756**, 144874 (2020).
70. Abi-Mosleh, L., Infante, R. E., Radhakrishnan, A., Goldstein, J. L. & Brown, M. S. Cyclodextrin overcomes deficient lysosome-to-endoplasmic reticulum transport of cholesterol in Niemann-Pick type C cells. *Proc. Natl. Acad. Sci. USA* **106**, 19316–19321 (2009).
71. Liu, B. et al. Reversal of defective lysosomal transport in NPC disease ameliorates liver dysfunction and neurodegeneration in the npc1^{-/-} mouse. *Proc. Natl. Acad. Sci. USA* **106**, 2377–2382 (2009).
72. Yao, J. et al. Neuroprotection by cyclodextrin in cell and mouse models of Alzheimer disease. *J. Exp. Med.* **209**, 2501–2513 (2012).
73. Beckett, D. A. et al. Repeated administration of 2-hydroxypropyl-beta-cyclodextrin (HPbetaCD) attenuates the chronic inflammatory response to experimental stroke. *J. Neurosci.* **42**, 325–348 (2022).
74. Agrawal, N. et al. Neurofilament light chain in cerebrospinal fluid as a novel biomarker in evaluating both clinical severity and therapeutic response in Niemann-Pick disease type C1. *Genet. Med.* **25**, 100349 (2023).
75. Sharma, R. et al. Long-term administration of intravenous trappsol(R) Cyclo (HP-beta-CD) results in clinical benefits and stabilization or slowing of disease progression in patients with Niemann-Pick disease type C1: results of an international 48-week phase I/II trial. *Mol. Genet. Metab. Rep.* **36**, 100988 (2023).
76. Kunkel, T. J. et al. The cholesterol transporter NPC1 is essential for epigenetic regulation and maturation of oligodendrocyte lineage cells. *Nat. Commun.* **14**, 3964 (2023).
77. Greensmith, L. & Bryson, J. B. The cholesterol depleting agent, (2-Hydroxypropyl)-ss-cyclodextrin, does not affect disease progression in SOD1(G93A) mice. *Amyotroph. Lateral Scler. Frontotemporal. Degener.* **25**, 1–7 (2023).
78. Proniuk, S. & Blanchard, J. Influence of degree of substitution of cyclodextrins on their colligative properties in solution. *J. Pharm. Sci.* **90**, 1086–1090 (2001).
79. Kislinger, G. et al. ATUM-FIB microscopy for targeting and multi-scale imaging of rare events in mouse cortex. *STAR Protoc.* **1**, 100232 (2020).
80. Harris, C. R. et al. Array programming with NumPy. *Nature* **585**, 357–362 (2020).
81. Bradski, G. The OpenCV Library. *Dr Dobb's Journal of Software Tools* (The OpenCV Library, 2000).
82. van der Walt, S. et al. scikit-image: image processing in Python. *PeerJ* **2**, e453 (2014).
83. Stringer, C., Wang, T., Michaelos, M. & Pachitariu, M. Cellpose: a generalist algorithm for cellular segmentation. *Nat. Methods* **18**, 100–106 (2021).
84. Martelotto, L. G. Frankenstein's protocol for nuclei isolation from fresh and frozen tissue for snRNAseq V.2. *protocols.io* (2020).
85. Hao, Y. et al. Integrated analysis of multimodal single-cell data. *Cell* **184**, 3573–3587.e3529 (2021).
86. Korsunsky, I. et al. Fast, sensitive and accurate integration of single-cell data with Harmony. *Nat. Methods* **16**, 1289–1296 (2019).
87. Zappia, L. & Oshlack, A. Clustering trees: a visualization for evaluating clusterings at multiple resolutions. *GigaScience* **7**, giy083 (2018).

88. Franzén, O., Gan, L.-M. & Björkegren, J. L. M. PanglaoDB: a web server for exploration of mouse and human single-cell RNA sequencing data. *Database* **2019**, baz046 (2019).
89. Cembrowski, M. S., Wang, L., Sugino, K., Shields, B. C. & Spruston, N. Hipposeq: a comprehensive RNA-seq database of gene expression in hippocampal principal neurons. *eLife* **5**, e14997 (2016).
90. Amezquita, R. A. et al. Orchestrating single-cell analysis with Bioconductor. *Nat. Methods* **17**, 137–145 (2020).
91. Love, M. I., Huber, W. & Anders, S. Moderated estimation of fold change and dispersion for RNA-seq data with DESeq2. *Genome Biol.* **15**, 550 (2014).
92. Dhingra, A. et al. Automated production of human induced pluripotent stem cell-derived cortical and dopaminergic neurons with integrated live-cell monitoring. *J. Vis. Exp.* **162**, e61525 (2020).
93. Czuppa, M. et al. Drug screen in iPSC-Neurons identifies nucleoside analogs as inhibitors of (G4C2)_n expression in C9orf72 ALS/FTD. *Cell Rep.* **39**, 110913 (2022).
94. Strauss, T. et al. iPS cell-based model for MAPT haplotype as a risk factor for human tauopathies identifies no major differences in TAU expression. *Front. Cell Dev. Biol.* **9**, 726866 (2021).
95. Janjic, A. et al. Prime-seq, efficient and powerful bulk RNA sequencing. *Genome Biol.* **23**, 88 (2022).

Acknowledgements

We acknowledge funding from the Deutsche Forschungsgemeinschaft (DFG, German Research Foundation) SyNergy EXC 2145—390857198 (D.E., M.S., E.B., G.K., Q.Z.), the Thierry Latran foundation (DE), a Sanofi iAward (DE), European Research Council (ERC) Starting Grant (C9-Immunity, 101117710, QZ) and the Horizon Europe Framework Program (HORIZON) under grant agreement 101057649 (GA-VAX) (D.E. and Q.Z.). S.F. was supported by the DFG Research Infrastructure NGS_CC (project 407495230) as part of the Next Generation Sequencing Competence Network (project 423957469). NGS analyzes were carried out at the Competence Centre for Genomic Analysis (Kiel). We thank Meike Michaelson for cryostat sectioning, Martina Fetting for input on the electron microscopy, and Christian Haass for providing the Simoa platform for serum NfL measurements. We thank Irina Dudanova, Christian Haass, Timothy Hammond, and Veit Hornung for helpful discussions. We thank TargetALS for providing RNAseq data from ALS patients and controls.

Author contributions

A.R., N.H., D.O., and D.E. conceived the project. A.R., Z.I.G., N.H., D.O., E.B., O.G., M.S., S.L., and D.E. designed research. A.R., V.K.-J., Z.I.G., Q. Zeng, G.K., H.B.I., T.K., L.R.P., S.F., K.D.L., A.J. performed the experiments with support from J. Koppenbrink, J. Knogler, D.F., B.N., E.K., G.G., A.D.,

C.Y., Q. Zhou. A.R., F.B., G.K., T.K., L.R.P., E.B., A.J., T.A., and D.E. analyzed data. The work was supervised by W.E., M.S., S.L., and D.E. The manuscript was written by D.E. and A.R. with contributions from all authors.

Funding

Open Access funding enabled and organized by Projekt DEAL.

Competing interests

L.R.P., N.H., and D.O. are employees of Sanofi, but Sanofi is not actively developing CD-based therapeutics. The remaining authors declare no competing interests.

Additional information

Supplementary information The online version contains supplementary material available at <https://doi.org/10.1038/s41467-025-58634-4>.

Correspondence and requests for materials should be addressed to Dieter Edbauer.

Peer review information *Nature Communications* thanks the anonymous reviewers for their contribution to the peer review of this work. A peer review file is available.

Reprints and permissions information is available at <http://www.nature.com/reprints>

Publisher's note Springer Nature remains neutral with regard to jurisdictional claims in published maps and institutional affiliations.

Open Access This article is licensed under a Creative Commons Attribution 4.0 International License, which permits use, sharing, adaptation, distribution and reproduction in any medium or format, as long as you give appropriate credit to the original author(s) and the source, provide a link to the Creative Commons licence, and indicate if changes were made. The images or other third party material in this article are included in the article's Creative Commons licence, unless indicated otherwise in a credit line to the material. If material is not included in the article's Creative Commons licence and your intended use is not permitted by statutory regulation or exceeds the permitted use, you will need to obtain permission directly from the copyright holder. To view a copy of this licence, visit <http://creativecommons.org/licenses/by/4.0/>.

© The Author(s) 2025

Ali Rezaei^{1,2,3}, Virág Kocsis-Jutka^{1,17}, Zeynep I. Gunes^{1,2,3,4,5,17}, Qing Zeng^{1,3,17}, Georg Kislinger^{1,2}, Franz Bauernschmitt^{2,4,5}, Huseyin Berkcan Isilgan¹, Laura R. Parisi⁶, Tuğberk Kaya^{1,2,7}, Sören Franzenburg⁸, Jonas Koppenbrink¹, Julia Knogler¹, Thomas Arzberger^{9,10}, Daniel Farny¹, Brigitte Nuscher¹¹, Eszter Katona^{1,2,3}, Ashutosh Dhingra¹², Chao Yang¹, Garyfallia Gouna^{1,3,13}, Katherine D. LaClair¹, Aleksandar Janjic¹⁴, Wolfgang Enard¹⁴, Qihui Zhou^{1,2}, Nellwyn Hagan⁶, Dmitry Ofengeim⁶, Eduardo Beltrán^{2,4,5}, Ozgun Gokce^{2,3,7,15}, Mikael Simons^{1,2,3,13}, Sabine Liebscher^{2,3,4,5,16} & Dieter Edbauer^{1,2,3} ✉

¹German Center for Neurodegenerative Diseases (DZNE), Munich, Germany. ²Munich Cluster of Systems Neurology (SyNergy), Munich, Germany. ³Ludwig-Maximilians-Universität (LMU) Munich, Graduate School of Systemic Neurosciences (GSN), Munich, Germany. ⁴Institute of Clinical Neuroimmunology, Klinikum der Universität München, Ludwig Maximilians University Munich, Munich, Germany. ⁵Biomedical Center, Ludwig Maximilians University Munich, Munich, Germany. ⁶Sanofi, Rare and Neurologic Diseases, Cambridge, MA, USA. ⁷Department of Neurodegenerative Diseases and Geriatric Psychiatry, University Hospital Bonn, Bonn, Germany. ⁸Institute of Clinical Molecular Biology, Kiel University, Kiel, Germany. ⁹Center for Neuropathology and Prion Research, University Hospital, LMU Munich, Munich, Germany. ¹⁰Department of Psychiatry and Psychotherapy, University Hospital, LMU Munich, Munich, Germany. ¹¹Chair of Metabolic Biochemistry, Biomedical Center (BMC), Faculty of Medicine, Ludwig-Maximilians-Universität Munich,

Munich, Germany. ¹²German Center for Neurodegenerative Diseases (DZNE), Tübingen, Germany. ¹³Institute of Neuronal Cell Biology, Technical University Munich, Munich, Germany. ¹⁴Anthropology and Human Genomics, Faculty of Biology, Ludwig-Maximilians Universität München, Munich, Germany. ¹⁵Institute for Stroke and Dementia Research, University Hospital of Munich, LMU Munich, Munich, Germany. ¹⁶Institute of Neurobiochemistry, Medical University of Innsbruck, Innsbruck, Austria. ¹⁷These authors contributed equally: Virág Kocsis-Jutka, Zeynep I. Gunes, Qing Zeng. ✉ e-mail: dieter.edbauer@dzne.de